Experimental Section

Materials

Lead iodide (PbI_2, 99.99%), lead bromide ($PbBr_2$, >98.0%), and bathocuproine (BCP, 99%) were purchased from Tokyo Chemical Industry Co., Ltd (TCI). Methylammonium bromide (MABr, >99.99%), formamidinium iodide (FAI, >99.99%), methylammonium chloride (MACl, 99.99%), and phenethylammonium iodide (PEAI) were purchased from Greatcell Solar. Phenyl-C61-butyric acid methyl ester (PCBM, ≥99.95%) and C_{60} was purchased from 1-Materials. Nickel(II) 2-ethylhexanoate 78% (in 2-Ethylhexanoic acid), N,N-dimethylformamide (DMF, 99.8%), dimethyl sulfoxide (DMSO, 99.9%), chlorobenzene (CB, 99.9%), isopropanol (IPA, 99.5%), cesium iodide (CsI, 99.999%), tert-Butanol (t-BuOH, anhydrous, ≥99.5%), anisole (anhydrous, 99.7%), hexane (Laboratory Reagent, ≥95%), ammonium fluoride (NH_4F, ≥99.99%), 3-mercaptobenzoic acid (3-MBA, 95%), thiophenol (99%), and benzoic acid (99.5%) were purchased from Sigma-Aldrich. Potassium hydroxide (KOH, 85%) was purchased from Alfa Aesar. Ethylene glycol (99.5%) was purchased from SAMCHUN. Di-tetrabutylammonium cis-cis(isothiocyanato) bis(2,2'-bipyridyl-4,4'-dicarboxylato) ruthenium (II) (N719 dye, >97 %) was purchased from Ossila.

The synthesis of adducts

To prepare the adduct phase. The experiment was conducted in a process based on antisolvent. For the PbI_2-based adducts, 0.31 M was dissolved with equivalent molar ratio of 3-MBA or BA in DMF solvetn and srirred for overnight before use. Then the solution was spin-coated on ITO substrate in 2000 r.p.m. for 30s. At the 10 second of spinning, 300 µl of chlorobenzene was dripped onto the substrate. The as-coated films were subsequently annealed on a hotplate at 70 °C for 10 min to eliminate residual DMF solvent.

The preparation of perovskite solutions

1.3 M $Cs_{0.05}(FA_{0.85}MA_{0.15})_{0.95}Pb(I_{0.85}Br_{0.15})_3$ perovskite precursor solutions were constructed in 1 ml co-solvent of DMF/DMSO (v/v=4/1). For the target perovskite, 1.6 mg ml^{-1} of 3-MBA was added into the precursor solution. 1.5 M $Cs_{0.05}FA_{0.92}MA_{0.03}PbI_{2.97}Br_{0.03}$ perovskite precursor solution was prepared along with 10 mol% of MACl. For the target perovskite, 0.1 mg ml^{-1} of 3-MBA was added into the precursor solution.

Device fabrication

The transparent conducting oxide glass substrates, fluorine-doped tin oxide (FTO) glass was used for the substrate. The glass was sequentially washed by bath type sonication with deionized water, acetone, and IPA for 10 min. After drying for 12 h in the oven at 70 °C, Ni layer (40 nm) was deposited on the rinsed FTO glass via a RF sputter (SRN-110). Anodization method (bottom-up process) was adopted for the preparation of NiO_x thin film. The detailed methods were included in our previous work.[1]

The A-NiO films were treated with an organometallic dye molecule (N-719 dye) on it to reduce surface traps and facilitate charge transport. More importantly, this inhibits hazard redox reaction between NiO_x and perovskite. 1.5 mg ml^{-1} of N-719 dye in DMF/t-BuOH (v/v=1/1) was spin-coated onto the A-NiO film at 2000 rpm for 30 s. The N-719 treated substrates were transferred to the N_2 glovebox immediately. It should be noted that all subsequent processes were conducted in a nitrogen glove box (O_2, H_2O < 0.1 ppm). Before coating the perovskite, samples were cleaned by dropping DMF solvent at 4000 rpm for 30 s to remove the residual N-719 which are not anchored to the A-NiO. For the perovskite layer preparation, 40 µL of the perovskite precursor was coated on the substrates. Afterwards, a spin-coating procedure of 1000 rpm for 10 s and 5000 rpm for 20 s was progressed. Then, 150 µL of anisole was dripped within one second at 5s before the end of last procedure. After spin-coating, films were

annealed at 100 ℃ for 30 min. For the surface defect passivation, PEAI (0.7 mg ml^{-1} in IPA) was dynamically dropped during spin-coating, in which spin speed and duration were optimized to 5000 rpm for 30 s. The devices were dynamically spin-coated to 2000 rpm for 30 s for electron transport layer, PCBM (20 mg ml^{-1} in CB) and heated at 100 °C for 10 min. In final step, saturated BCP solution (5.0 mg ml^{-1} in IPA) filtered with PTFE 0.2 µm, was spin coated at 4000 rpm for 30 s. Finally, 100 nm of Ag was thermally deposited under low vacuum condition (< 5×10^{-6} torr).

For the stability test, 30 nm of C_{60} as electron transport layer was thermally evaporated on the perovskite film under a high vacuum of ~ 5×10^{-6} torr. We replaced BCP with ALD-SnO_2 as a hole blocking layer. SnO_2 layer were obtained through the ALD of Tetrakis(dimethylamido)tin(IV) (TDMASn, UP Chemical Co., Ltd) precursor and H_2O (deionized water) reactant. The deposition process was carried out using a showerhead type ALD system (CN1 Co., Ltd, ATOMIC PREMIUM) at a temperature of 100 °C. A total of 130 ALD cycles were executed to achieve a controlled SnO_2. The sub-ALD cycle included precise steps: a 0.5-second dosing with the TDMASn precursor, followed by a 15-second purging step with N_2, then a 0.5-second dosing with H_2O reactant, and finally, a 15-second purging step with N_2.

Solar cell characterization

The current density-voltage (*J-V*) characteristics of solar cells were measured under one-sun illumination (AM 1.5 G) by a Newport Oriel Sol 3A solar simulator with Keithley 2400 source meter. The light intensity is calibrated with KG-5 filtered monosilicon standard cells, certified by the National Renewable Energy Laboratory. The *J-V* curves were obtained with reverse (1.25 V to -0.05 V) and forward scan direction (-0.05 V to 1.25 V) using an active area of 0.056 cm^2. The active area was determined by the metal aperture (0.056 cm^2). The *J-V* curves were

performed in ambient air. The external quantum efficiency measurement was conducted using a Newport Oriel Quanta X300 and Oriel Cornerstone 130 monochromator filter in ambient air.

Steady-state power conversion efficiency was carried out by using a Maximum power point (MPP) tracking system under continuous 100 mW cm^{-2} light intensity (AM 1.5 G) at ambient air. For thermal stability test, unencapsulated devices were heated at 85 °C in an nitrogen-filled glovebox and in humid condition (RH of 70 ± 5%), respectively. Before the measurement, the devices were cooled doown to room temperature. For ambient stability test, unencapsulated devices were stored in 25 °C and RH of 35 ± 5%. For MPP tracking under continuous light illumination, calibrated 1-sun light source with UV-free white LED was used. The unencapsulated devices were continuously measured under Perturb and Observe (P&O) algorithm.

Other characterization

Ultraviolet photoelectron spectroscopy (UPS) and X-ray photoelectron spectroscopy (XPS) was performed with a Thermo Scientific ESCALAB 250XiW. The XPS spectra were calibrated based on the C 1s peak at a binding energy of 284.5 eV. UPS characterization measurements were conducted the system equiped with He-discharge lamp (hv = 21.22 eV). Field emission scanning electron microscopy (FE-SEM) images were observed using a HITACHI SU8020. Tauc plot and Absorption spectra were obtained using Jasco V-770 UV-Vis-NIR Spectrophotometer. Fourier-Transform nuclear magnetic resonance spectrometry (FT-NMR) were recorded at 400 MHz, by using a Bruker Avance 400 NMR spectrometer, where ^{1}H-NMR were collected in a DMSO-d_6 deuterium solvent. XRD data were measured by employing an X-ray diffractometer

(Bruker D2 Phase). The photoluminescence (PL) spectra and decay curves were acquired on a FluoTime 300 (PicoQuant mbH) using a PicoHarp 300 as time-correlated single photon counting setup (TCSPC) and a pulsed laser diode with an excitation wavelength of 515 nm (LDH-P-C-520, PicoQuant GmbH).

Electrochemical impedance spectroscopy (EIS) was conducted by using a VSP potentiostat. Nyquist measurement was measured under dark condition at open circuit voltage bias from 1MHz to 100Hz. Mott-Schottky analysis was obtained in condition of a frequency at 10kHz. Fourier-transform infrared (FT-IR) spectroscopy were obtained by utilizing a Thermo Scientific Nicolet6700. The atomic force microscopy (AFM) and kelvin probe force microscopy (KPFM) results were obtained usng an XE7 AFM (Park Systems) with NSC-36 tip and lock-in amplifier (Stanford Research system, SR830). Absolute photoluminescence quantum yield (PLQY)s of perovskite films were measured using a Hamamatsu Photonics Quantaurus-QY Plus UV-NIR absolute PLQY spectrometer, equipped with a 3.3-inch spectralon-coated integrating sphere. For perovskite films, a reference spectrum was obtained with a glass substrate in empty laboratory quartz dish (diameter was 1 cm) placed at the center of integrating sphere, then the sample spectrum was obtained with the same cuvette filled with different films. A high power (150 W, 40% output) xenon lamp (Hamamatsu Photonics, L13685-01) with a 520 nm bandpass filter (bandwidth 50 nm) was used as excitation source for absolute QY measurement. Raman spectroscopy was conducted through XploRATM PLUS Raman spectrometer, HORIBA employing immersion objective lens (60x and 100x) with 785 laser.

Computational method

Our first-principles calculations of the structural and electronic properties of the perovskite crystal were performed using the density functional theory (DFT) as implemented in the

Cambridge Serial Total Energy Package (CASTEP). The generalized gradient approximation (GGA) of Perdew-Burke-Ernzerhof (PBE) was adopted for the exchange-correlation functional. The ultrasoft pseudopotentials were employed to describe electron-ion interactions, and van der Waals interactions were included using the empirical D3 dispersion correction method of Grimme. We set the cutoff energy to 500 eV, the energy tolerance to 10^{-6} eV, and the maximum force convergence criterion to 0.01 eV $Å^{-1}$. The Monkhorst–Pack *k*-point grid samplings was 6 × 6 × 6 for a primitive perovskite cell and 3 × 5 × 1 for the surfaces. A vacuum layer of 20 Å along the z-axis for each slab was added to decouple possible periodic interactions. In addition, DFT calculations of the isolated molecules were performed using the Gaussian 16 software package at the CAM-B3LYP/6-311G(*d*,2*p*) and LanL2DZ levels of theory. We calculated the theoretical NMR isotropic shielding constants (σ) using the GIAO DFT approach with the 6-311+G(*d*,*p*) basis set. To accurately account for the solvent environment, we employed an explicit-implicit solvent model in the GIAO-NMR calculations. To be specific, short-range hydrogen-bonding interactions were modeled by including one explicit DMSO molecule per amine proton, while other solvation effects were captured using the SMD implicit solvation model. Finally, chemical shifts (δ) were determined using the formula $\delta = \sigma_{ref} - \sigma$, where σ_{ref} represents the shielding constants of tetramethylsilane calculated at the same level of theory.

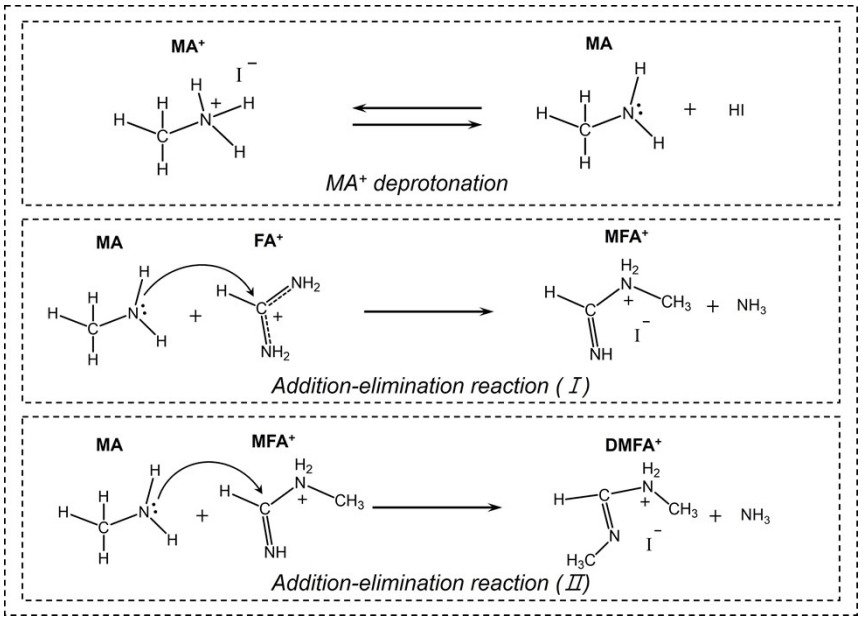

Figure S1. Schematic illustration of the major organic and iodide ion degradation mechanisms in perovskite precursor.[2] MFA^+ and $DMFA^+$ are methyl formamidinium ion and *N,N'*-dimethyl formamidinium ion, respectively.

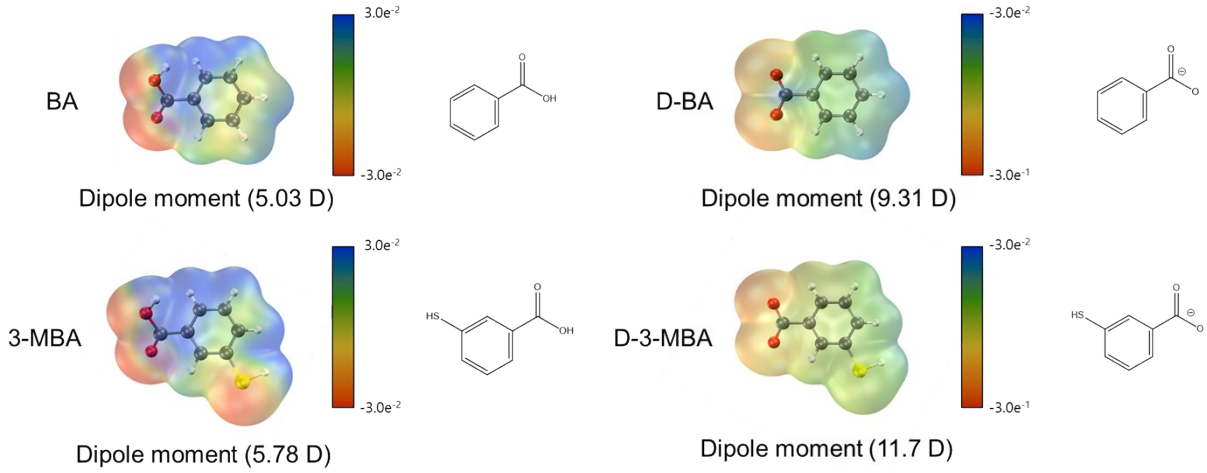

Figure S2. The chemical structure and corresponding calculated electrostatic potential (ESP) distributions of two passivators and their deprotonated forms. D is the Debye defined as the dipole moment.

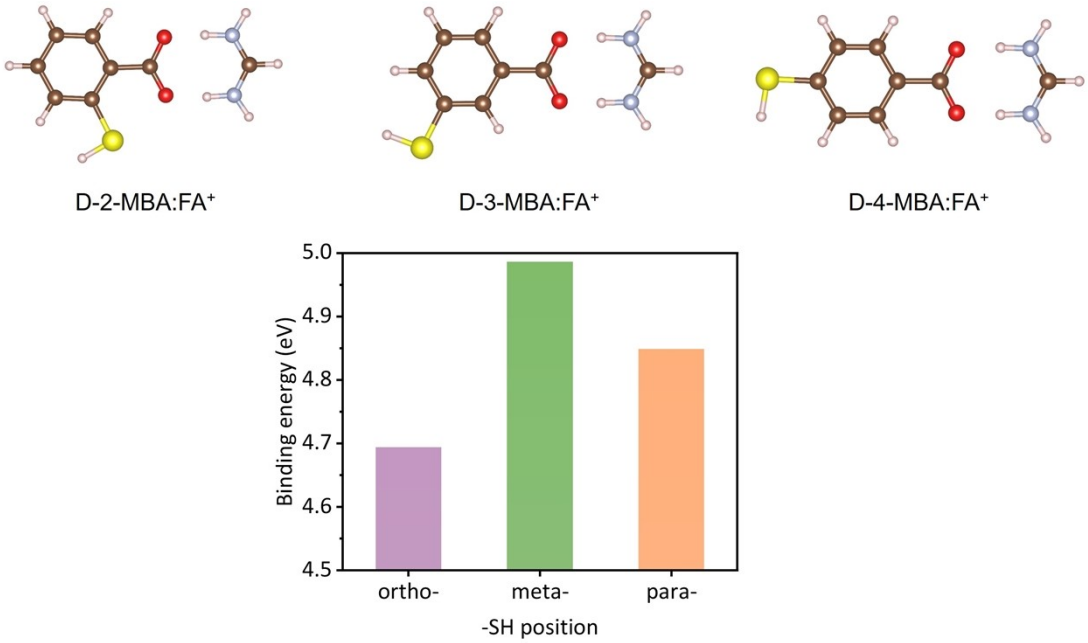

Figure S3. Binding energy between deprotonated regioisomers (different mercapto-benzoates) and NH_2^+ group of FA^+.

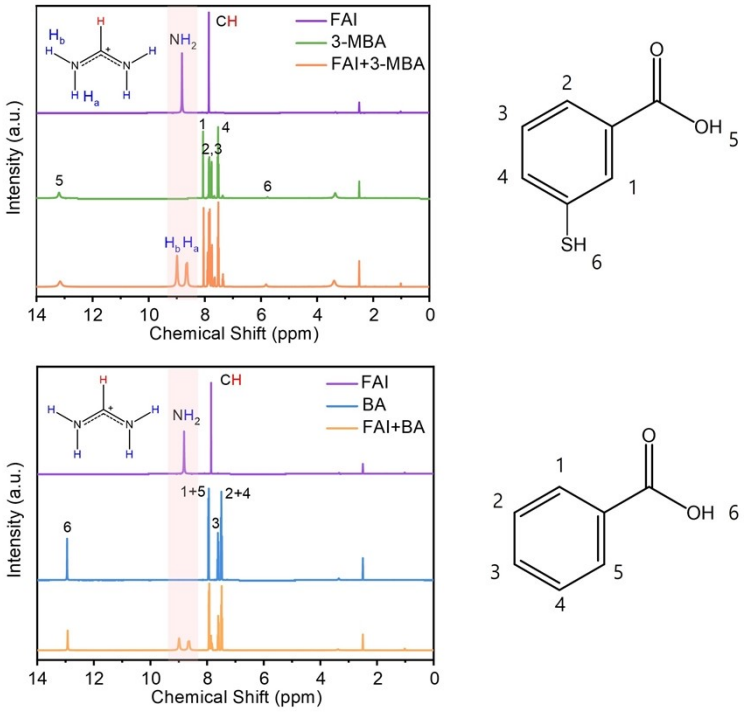

Figure S4. (a) ^{1}H-NMR spectra of FAI, 3-MBA and FAI+3-MBA mixtures (DMSO-d_6 solvent; 2.50 ppm), The molecule structure of 3-MBA, in which the proton numbers are denoted. (b) ^{1}H-NMR spectra of FAI, BA and FAI+BA mixtures (DMSO-d_6), The molecule structure of BA, in which the proton numbers are denoted.

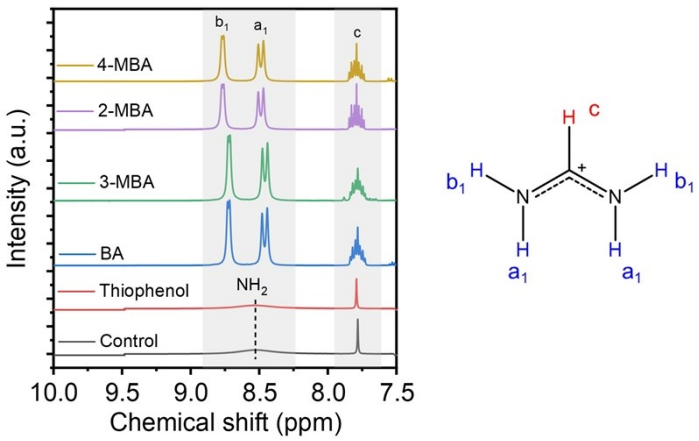

Figure S5. NMR spectra of perovskite precursors added with regioisomers (mercapto-benzoic acid), BA, and thiophenol

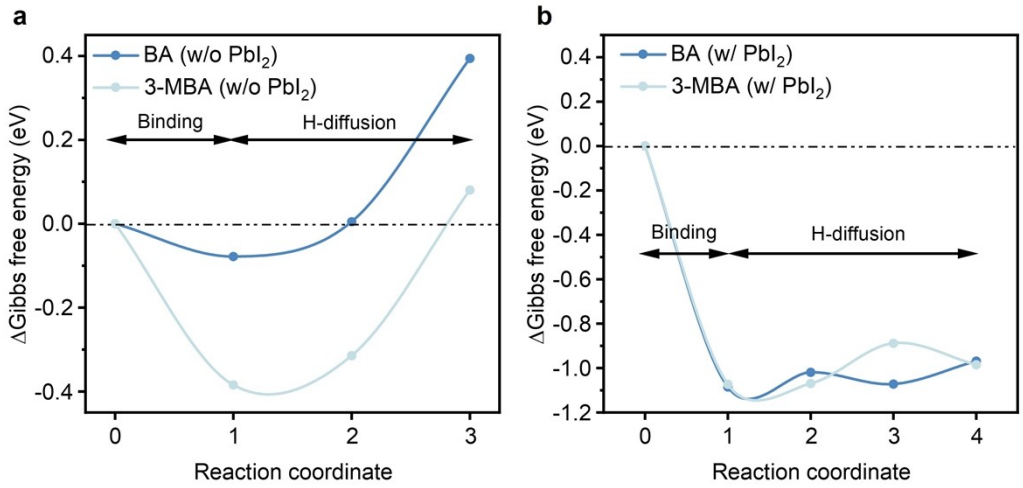

Figure S6. Gibbs free energy profiles for the dehydrogeneration of ligand molecules of BA and 3-MBA, both with (a) and without (b) the presence of PbI_2. These processes involve two consecutive reactions: intermolecular binding between the ligand (L) and solvent (i.e., DMF) molecules, followed by hydrogen diffusion from L to DMF, with the latter being the rate-determining step in both cases. For the direct dehydrogenation mechanism, the dehydrogeneration of BA by DMF, acting as a weak Brønsted base, shows a Gibbs' free energy change value (ΔG^0) of 0.39 eV, while the corresponding value for 3-MBA is only 0.08 eV. This calculation suggests that the deprotonation of 3-MBA is more favorable than that of BA, consistent with the experimental data presented in Fig. 1c. In contrast, the presence of PbI_2, significantly alters the reaction thermodynamics. PbI_2-assisted dehydrogenation processes are exothermic and spontaneous ($\Delta G_0 < 0$), primarily due to the strong coordination of Pb^{2+} with L, forming stable PbI-L complexes. These complexes exhibit a higher binding affinity to DMF compared to their individual components, as indicated in Step 1. This strong binding facilitates the deprotonation of L by DMF, which is further supported by the lower activation free energies observed compared to the direction dehydrogenation mechanism.

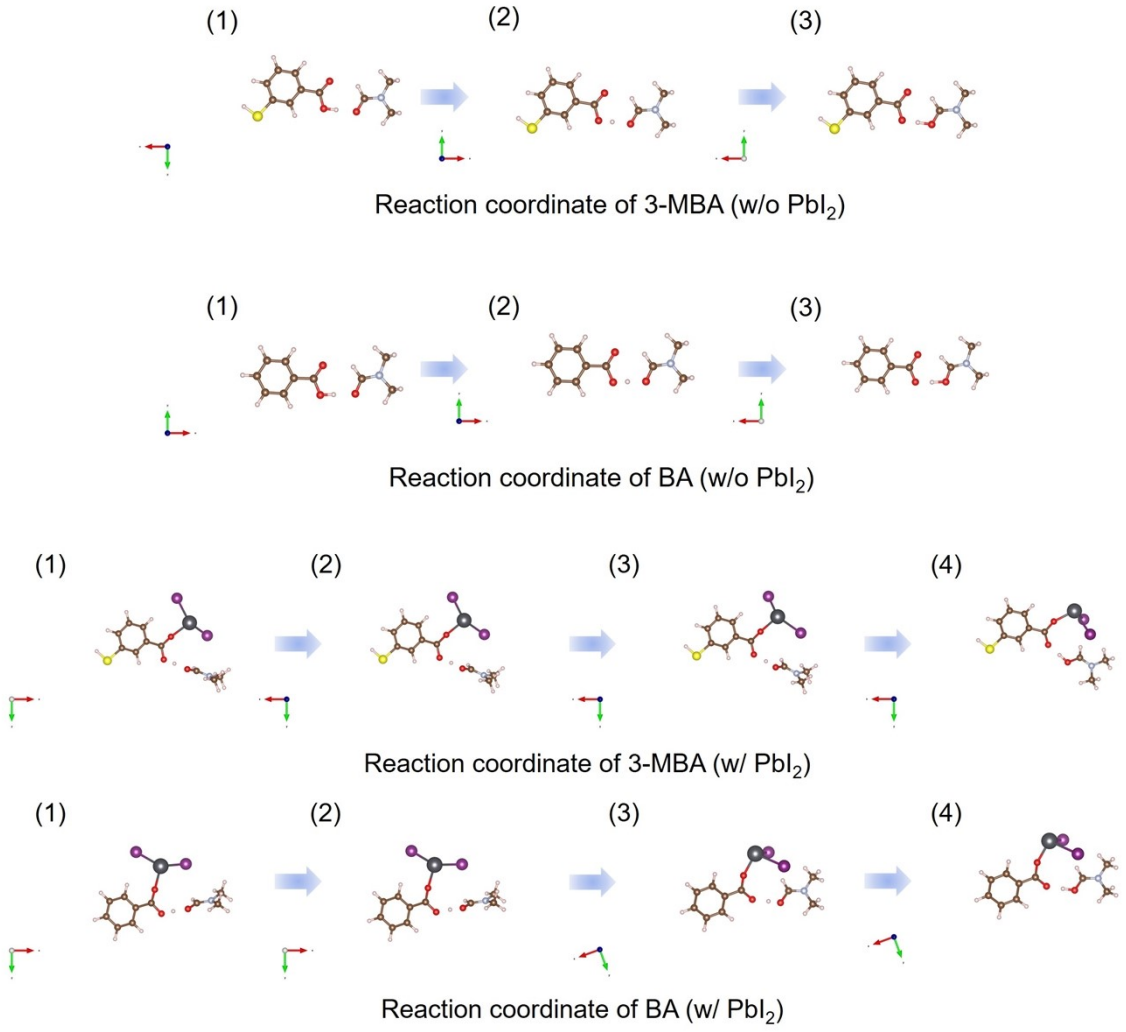

Figure S7. Geometry-optimized structures of intermediates, products, and transitions states for each reaction coordinates involved in the deprotonation of additives by DMF.

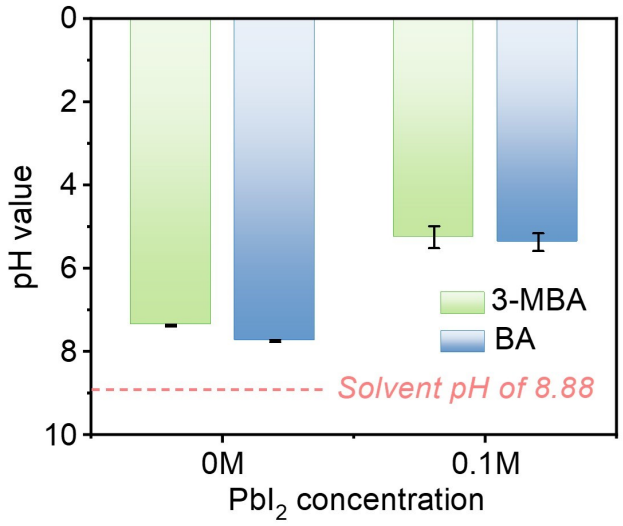

Figure S8. Evolution of pH value depending on the PbI_2 incorporation in additives solution (DMF/DMSO 4:1 mixture solvent).

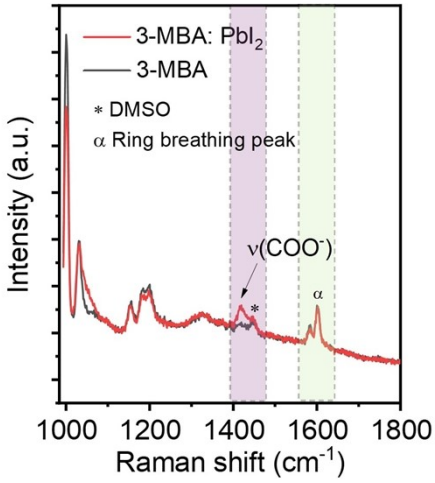

Figure S9. Raman spectra for the 3-MBA and 3-MBA with PbI_2. To assess the relative intensity of the carboxylate upon the addition of PbI_2, we calculated the area ratio of the $\nu(COO^-)$ band to the ring breathing mode (1590 cm^{-1}) in 3-MBA.

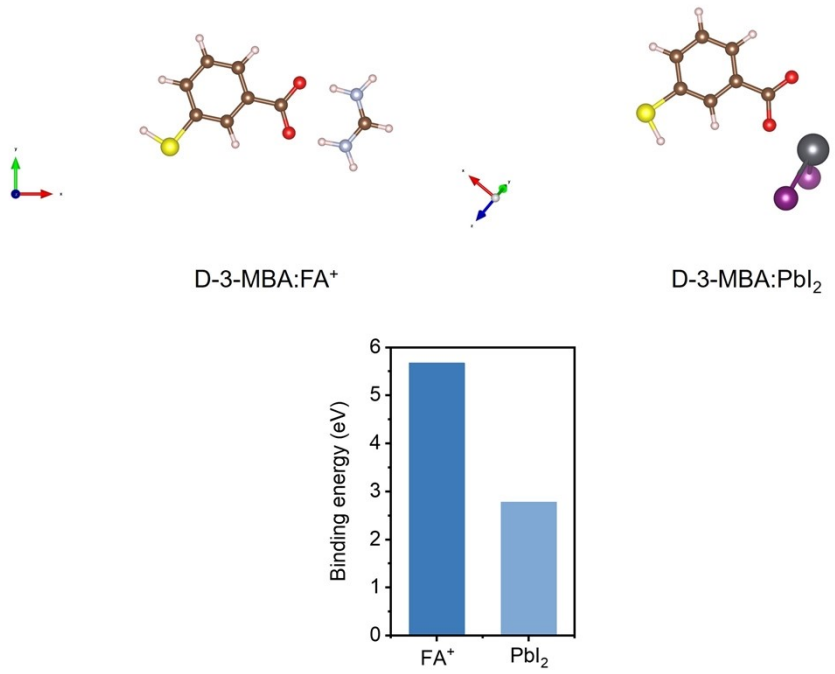

Figure S10. Binding energy of PbI_2 and FA^+ with D-3-MBA.

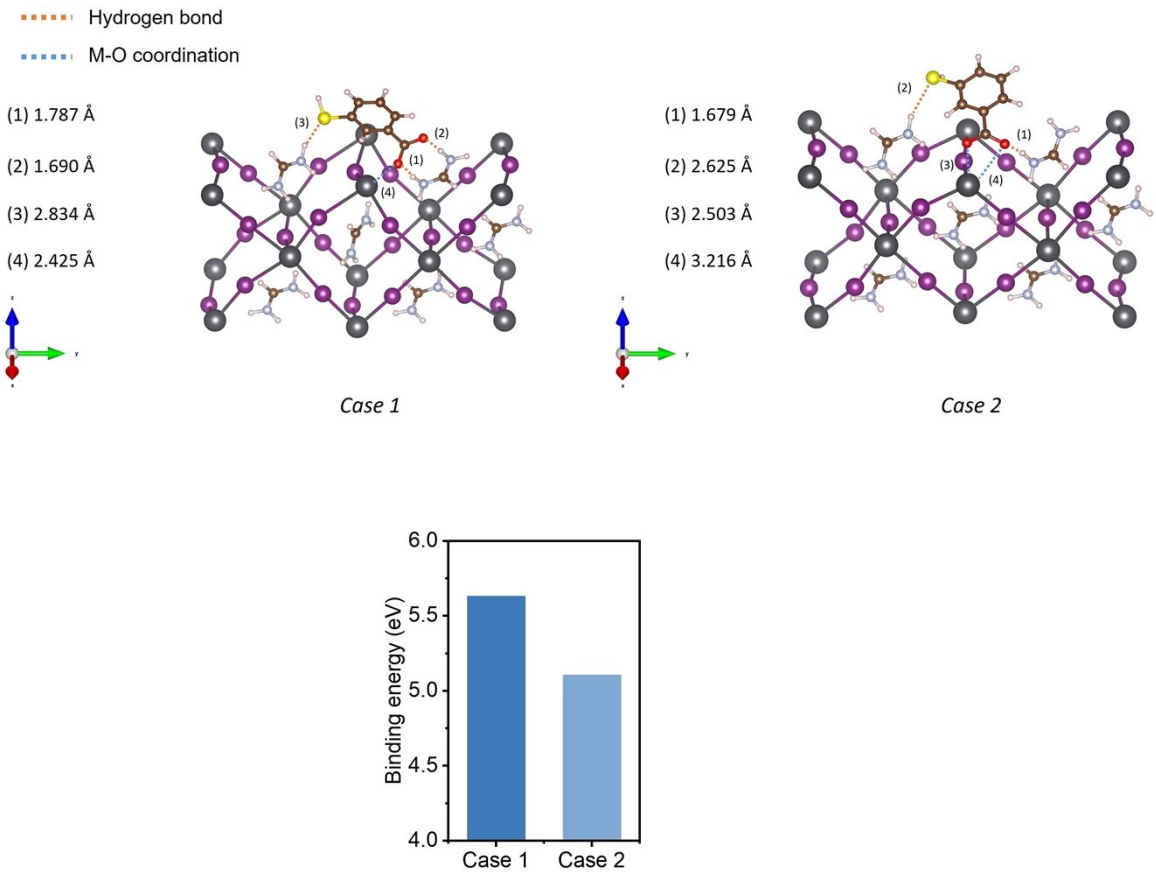

Figure S11. Optimized geometries of the (110) facet with both the organic component (FA^{+}) and the inorganic cage (PbI_6^{4-} octahedral framework), where for the case 1 and 2, D-3-MBA binds with hydrogen bonding and M-O coordination bonding and corresponding binding energy for the different optimized geometric cases.

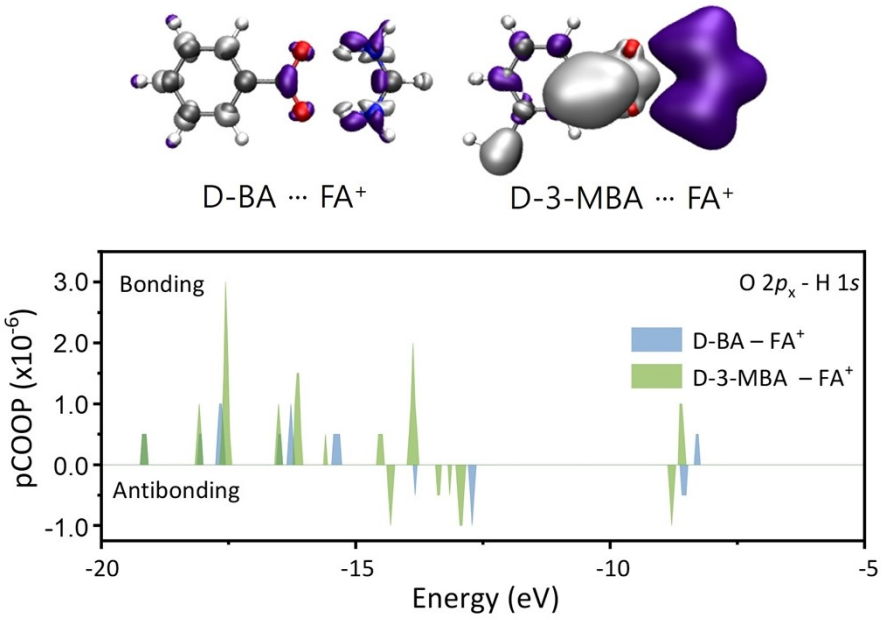

Figure S12. Electron density difference (EDD) of D-BA and D-3-MBA–FA^+ and corresponding projected crystal orbital overlap population (pCOOP) of the O-H bond (O $2p_x$–H 1*s*) in D-BA and D-3-MBA–FA^+.

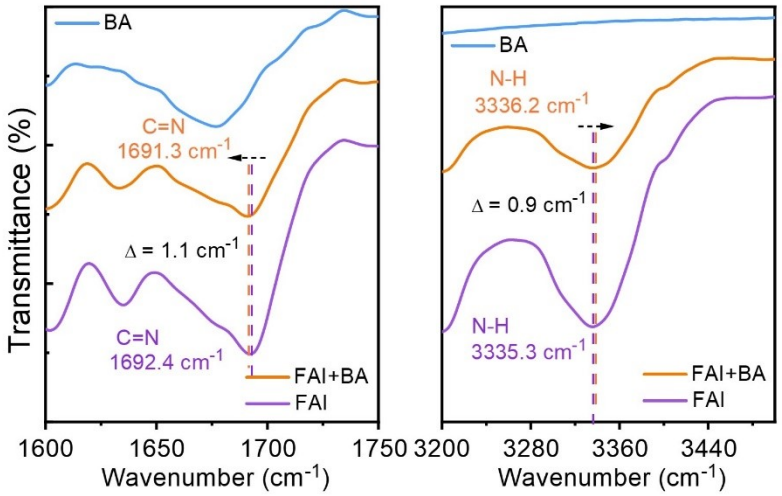

Figure S13. The Fourier transform infra-red (FTIR) spectra for the FAI, BA, and mixed FAI and BA. BA-treated FAI showed a lower shift representing C=N stretching vibration peaks to 1691.3 cm^{-1} (Δ=1.1 cm^{-1}), compared to that of the pure FAI (1692.4 cm^{-1}). For the NH_2^+ stretching vibration peaks of pure FAI (3335.3 cm^{-1}), the addition of BA shifted higher wavenumber to 3336.2 cm^{-1} (Δ=0.9 cm^{-1}).

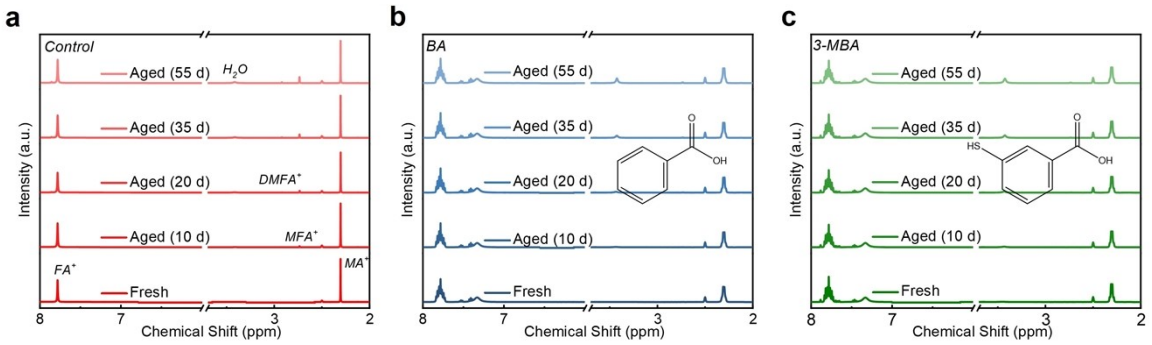

Figure S14. The nuclear magnetic resonance (^{1}H-NMR) spectra of (a) control perovskite precursors, (b) 3-MBA- and (c) BA-treated precursors tracked for 0d, 10d, 20d, 35d, and 55d. These solutions were maintained at room temperature and a relative humidity (RH) of 40 ± 5%.

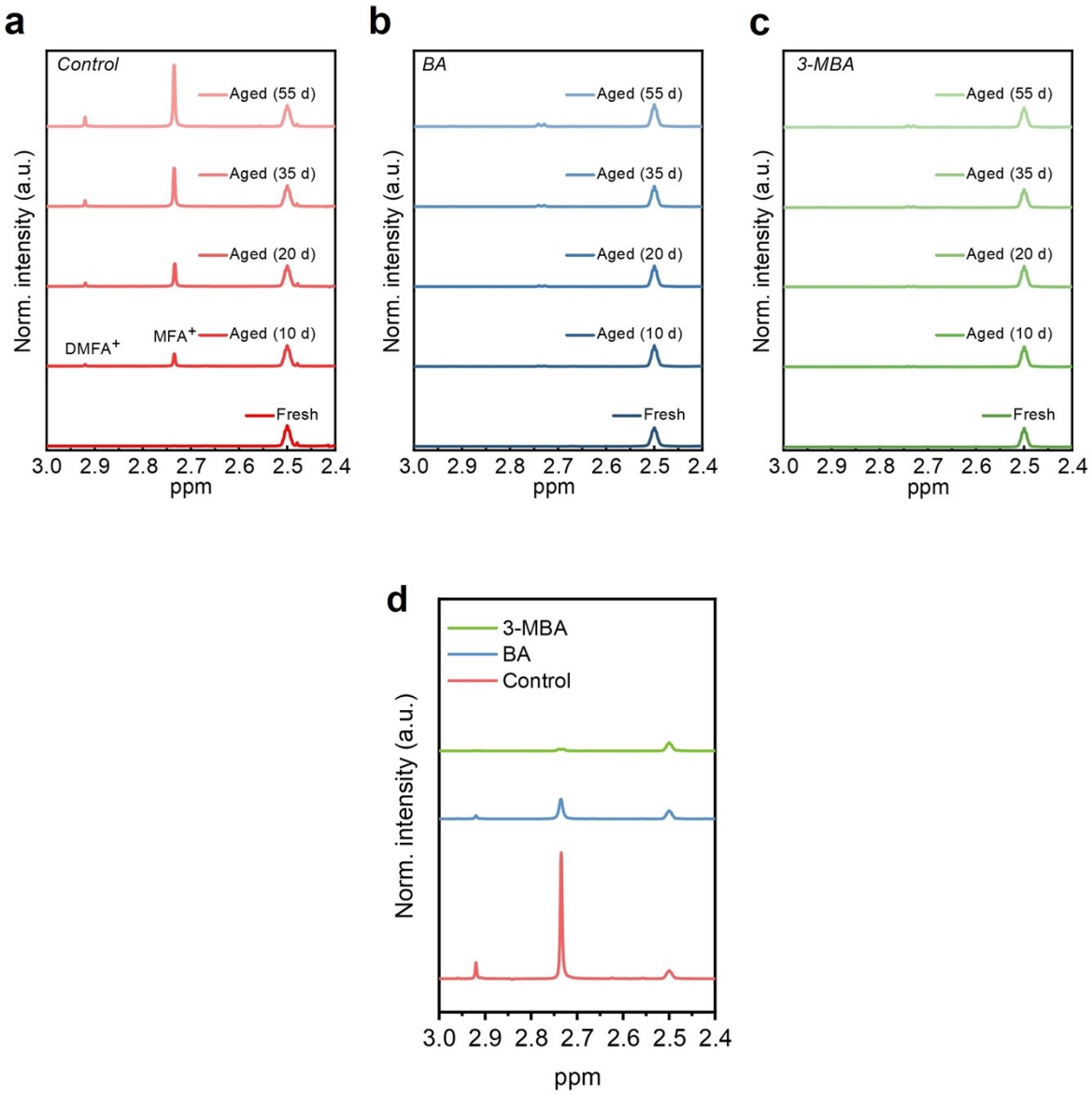

Figure S15. ^{1}H-NMR spectra representing the generation of large organic cations (MFA^{+} (2.77 ppm) and $DMFA^{+}$ (2.94 ppm)) of (a) control perovskite precursors, (b) 3-MBA- and (c) BA-treated precursors tracked for 0d, 10d, 20d, 35d, 55d, and (d) 140d.

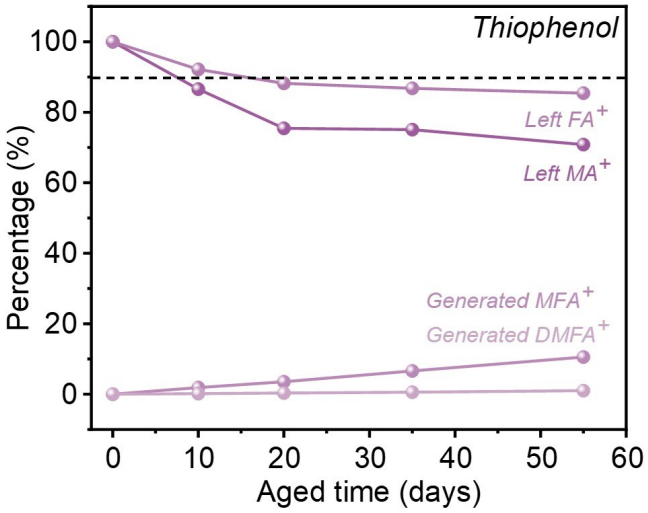

Figure S16. Evolution of main organic cations in thiophenol-treated perovskite solution, where we incorporated thiophenol as the same molar ratio with 3-MBA.

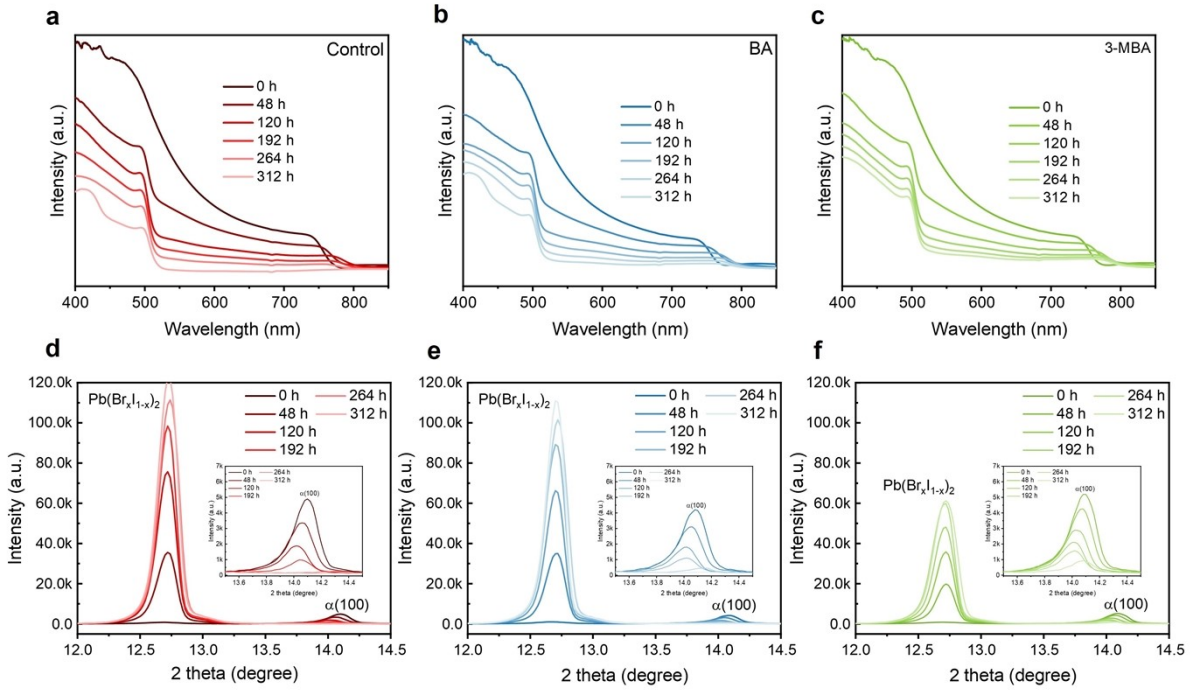

Figure S17. Ultraviolet-visible (UV-vis) absorption spectra of (a) control, (b) 3-MBA, and (c) BA-treated films annealing for 312h at 150 °C in N_2 environment. Corresponding X-ray diffraction (XRD) patterns (d), (e), (f) annealing for 0h, 48h, 120h, 192h, 264h, and 312h, respectively; The insets show the enlarged XRD patterns, indicating the evolution of the α(100) phase during thermally heated at 150 °C. In the case of the pristine sample, the absorption intensity of the α-phase completely vanished after 312 h. Furthermore, the $Pb(Br_xI_{1-x})_2$ peak at $2\theta \approx 12.7°$ exhibited a drastic increase after 312 h, concurrently with the complete disappearance of the α-phase peak at $2\theta \approx 14.2°$. Meanwhile, the 3-MBA-treated sample showed roughly delayed degradation, better than the BA-treated sample.

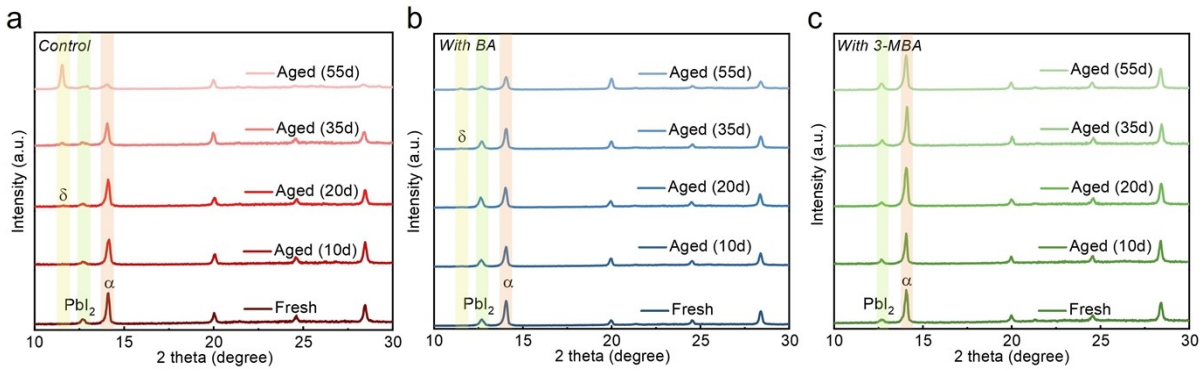

Figure S18. XRD patterns of (a) control, (b) BA-, and (c) 3-MBA- treated perovskite films using aged precursor for 0d, 20d, 35d, and 55d, respectively. Enlarged XRD patterns for the α-phase peaks.

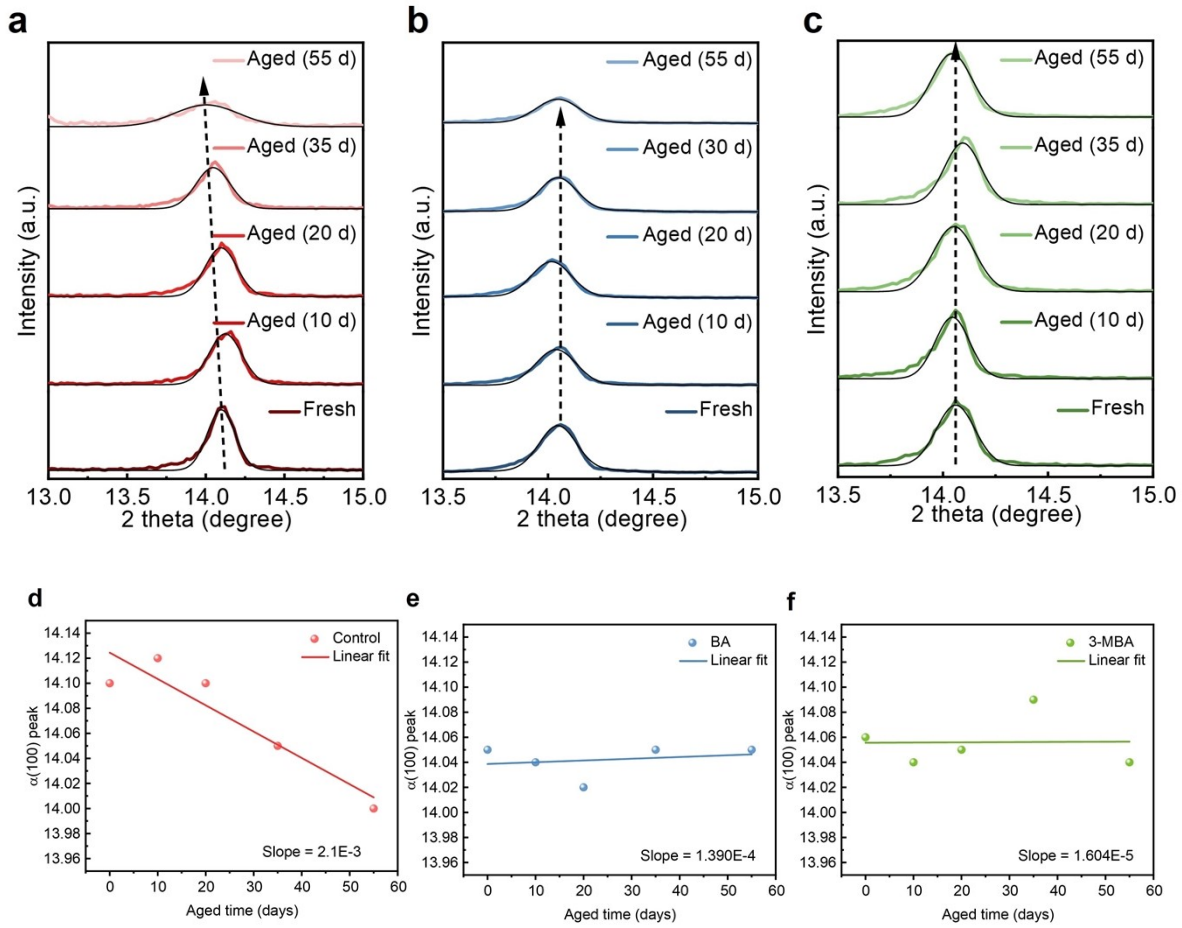

Figure S19. Evolution of α-phase peak from the XRD patterns of the (a), (d) control, (b), (e) BA-, and (c), (f) 3-MBA-treated perovskite films depending on storage time from 0d (fresh) to 55d. In contrast to the control precursor solution, the α-phase (100) facet peak in the BA-added precursor solution does not shift, which may indicate that the by-products affects a minimal part for degradation of BA included precursor.

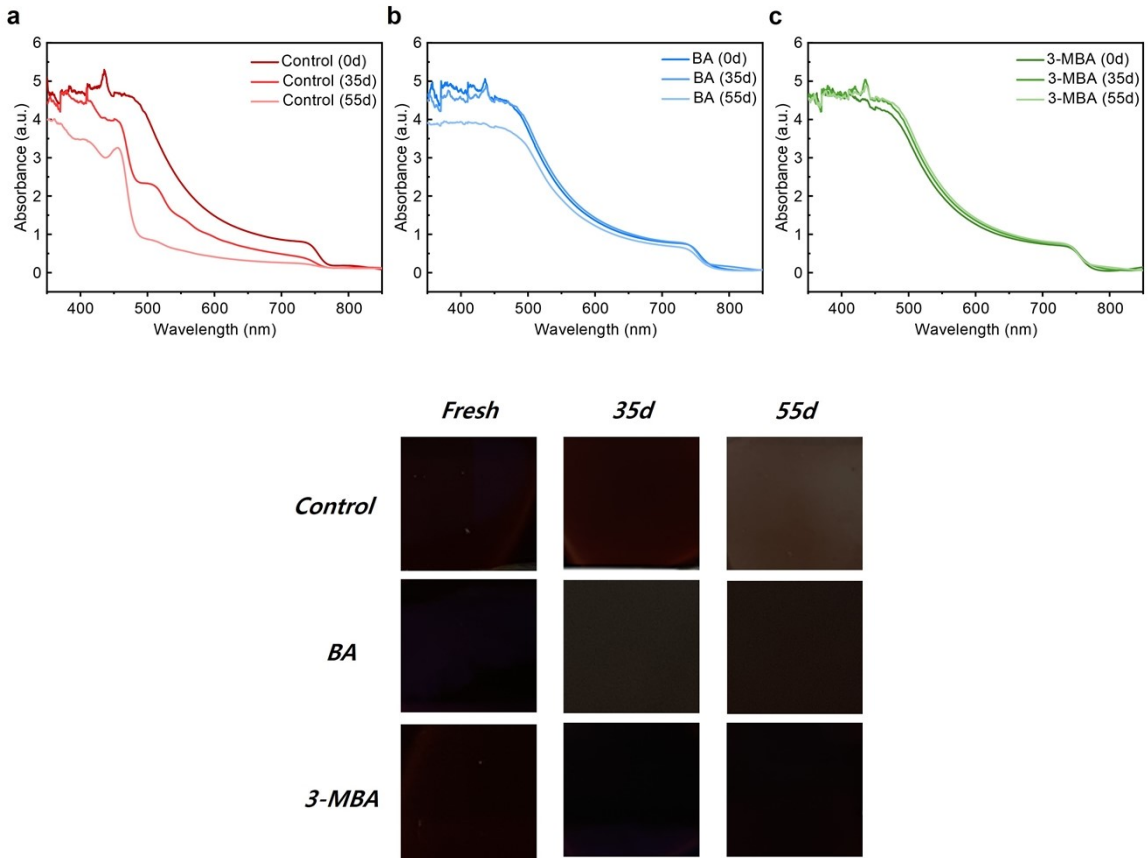

Figure S20. UV-vis absorption spectra of (a) control, (b) BA, and (c) 3-MBA-treated films using aged precursor for 0d, 35d, and 55d, respectively. Photographs corresponding the above films.

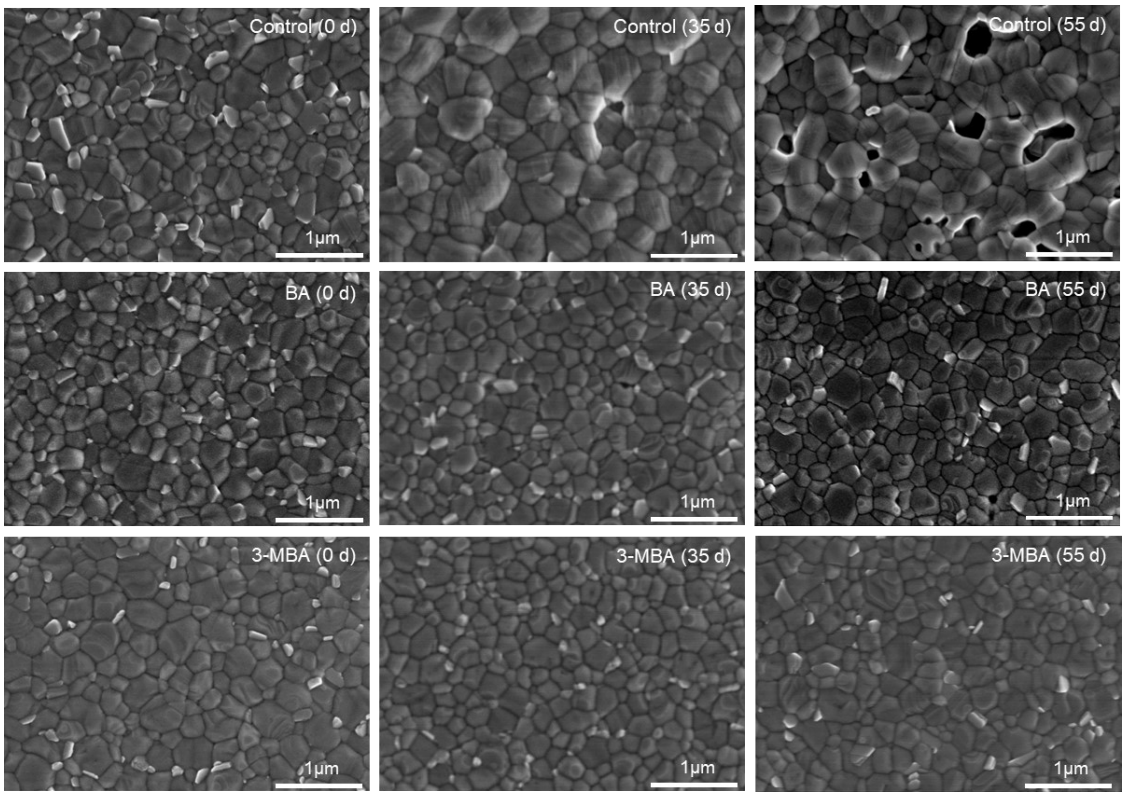

Figure S21. Top-view SEM images of control, 3-MBA, and BA-treated perovskite films using aged precursor for 0d, 35d, and 55d, respectively. The control perovskite film exhibits significant morphological degradation, including a large number of pin-holes and merged grains, as the aging time of the precursor increases. The BA-added perovskite film displays a reduced number of pin-holes; however, several pin-holes are still observed as the precursor ages.

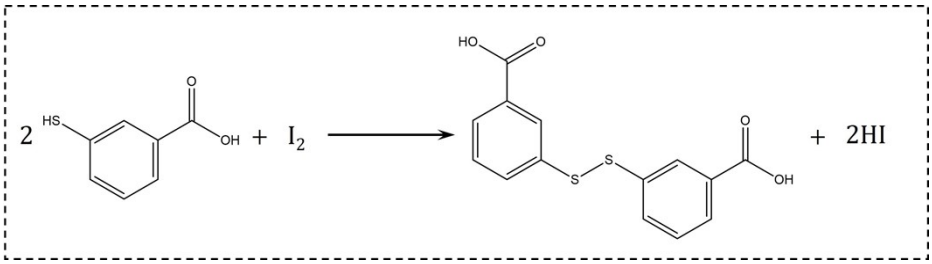

Figure S22. Proposed thiol to disulfide exchange reaction of 3-MBA.[3]

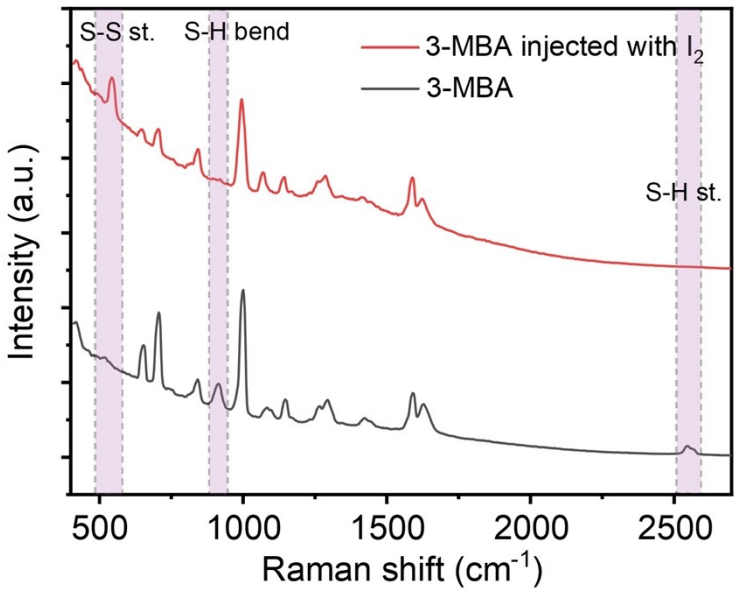

Figure S23. Raman spectra of 3-MBA and 3-MBA with I_2. (stretching is denoted as st.)

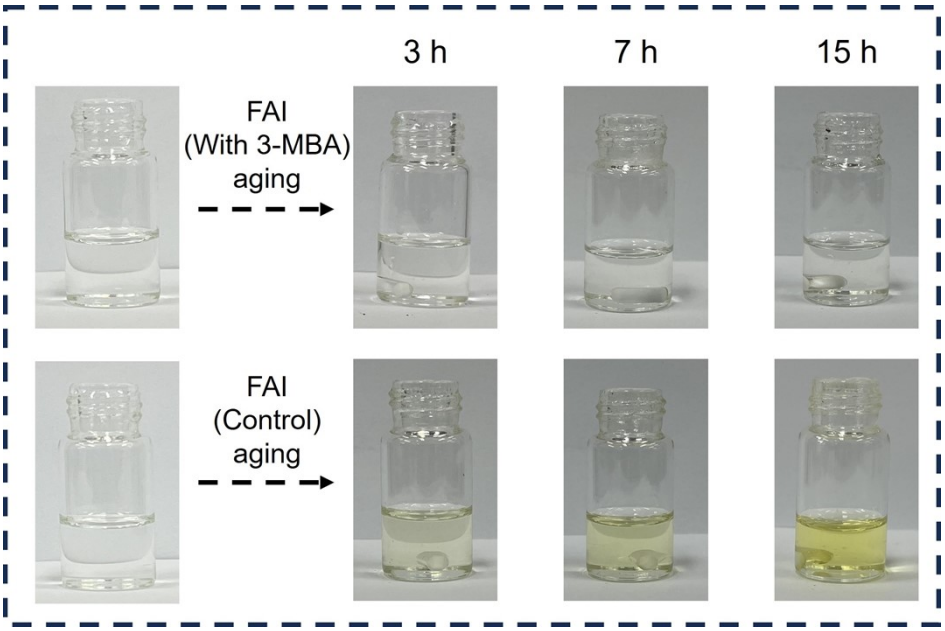

Figure S24. Photographs of vials for inspection of iodine generation in the pure FAI, and FAI+3-MBA solutions (DMF solvent).

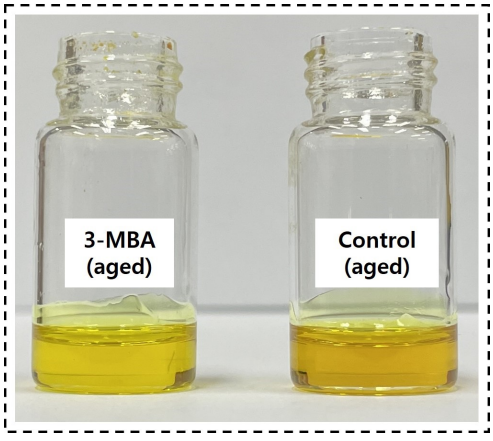

Figure S25. Aged precursor solution treated with and without 3-MBA after 4 days. The solution was stored with open cover at 60 °C under continuous stirring to accelerate the iodide oxidation reaction.

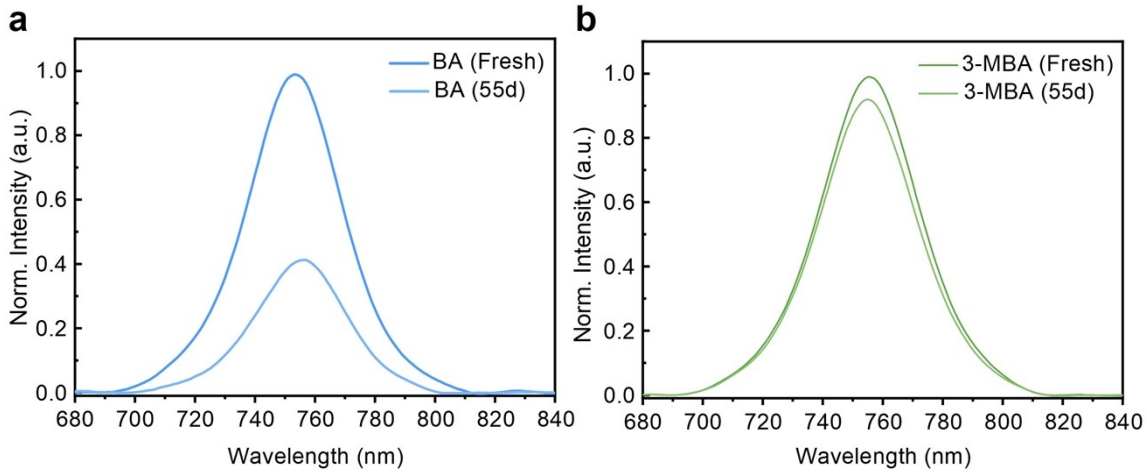

Figure S26. Normalized PL spectra for (a) fresh and aged BA-treated film (55 d) and (b) fresh and aged 3-MBA-treated film (55 d)

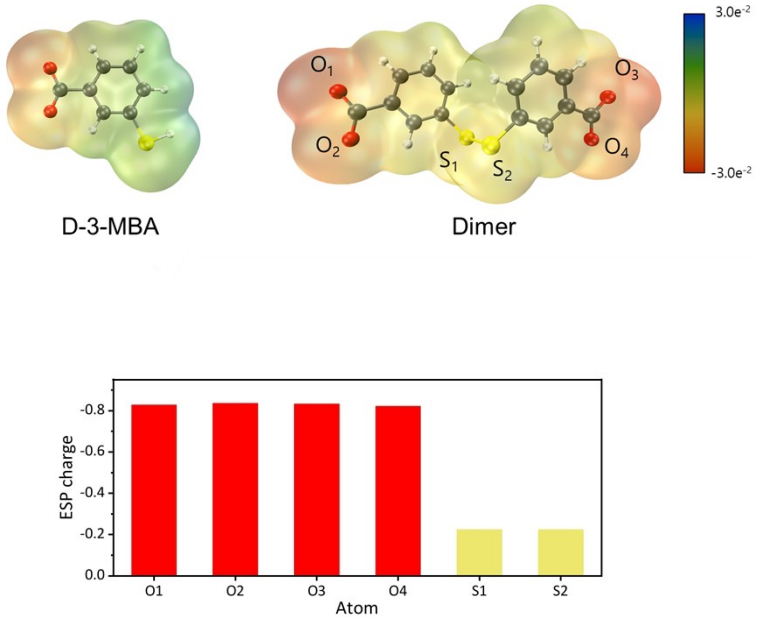

Figure S27. Simulated ESP distribution of the dimer derived from the thiol-disulfide oxidation of D-3-MBA (top) and its atomic ESP charges (bottom). Given these values, which are comparable to those of D-3-MBA, it can be expected that this dimer also has great potential for acting as a capping ligand for the surface passivation of the perovskite.

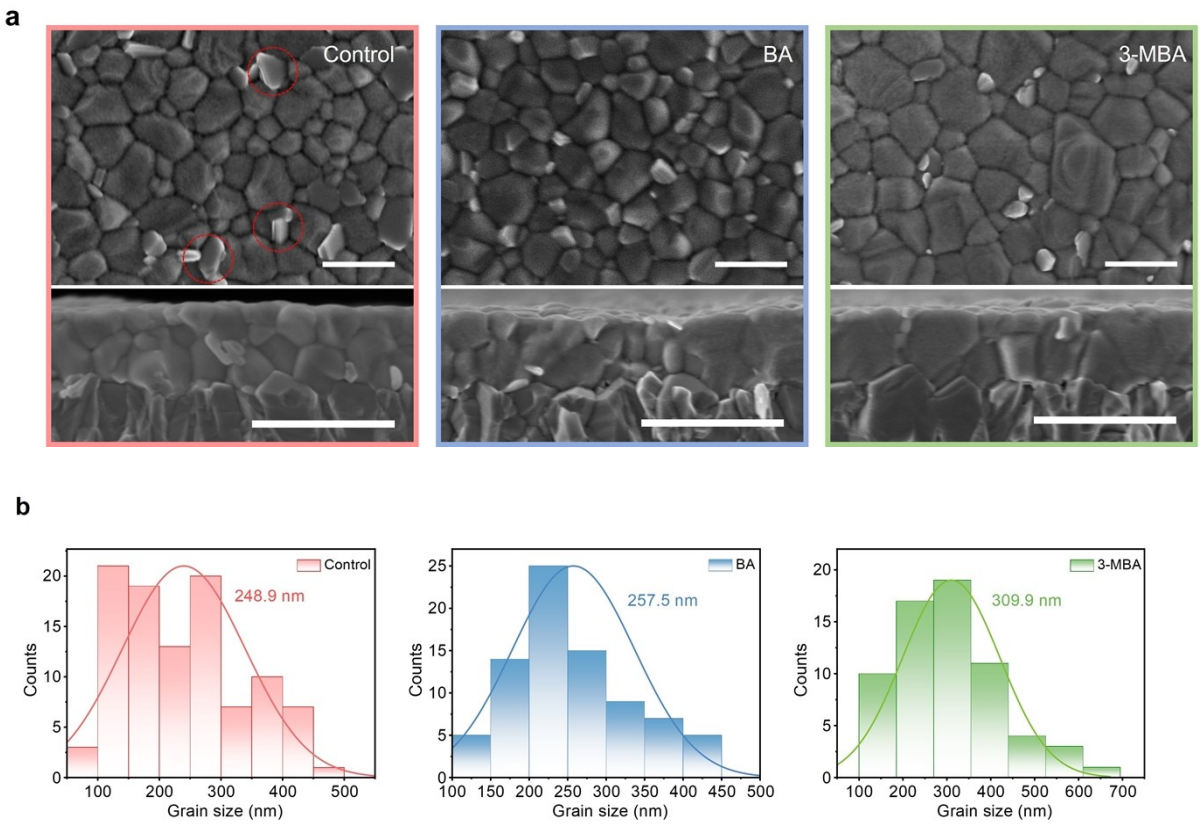

Figure S28. (a) Top-view SEM images and corresponding cross-sectional SEM images. (b) The size distribution of the grains. A minor increase in the average grain size of the BA-treated perovskite film may be attributed to the more acidic nature of the precursor.[4,5] The red circles indicate PbI_2 flakes.

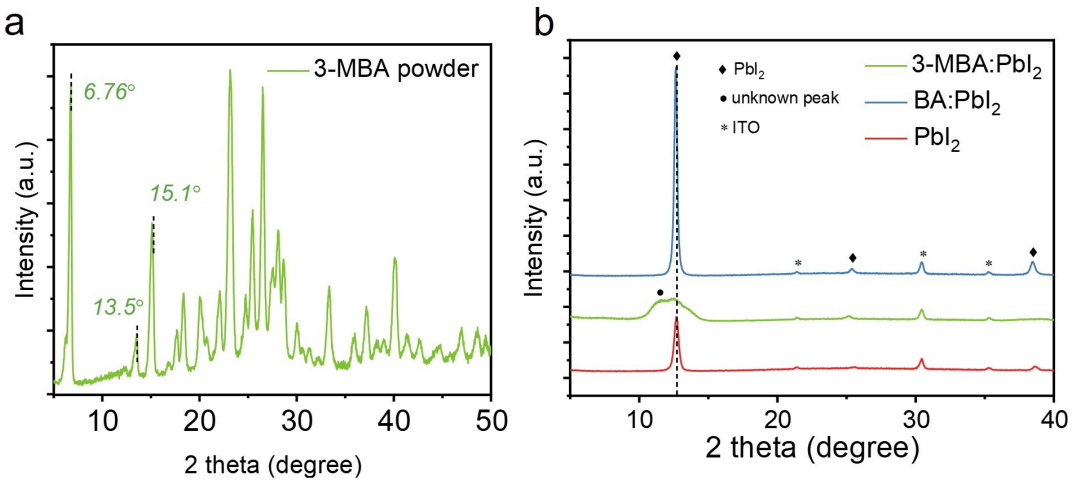

Figure S29. XRD patterns of (a) pure 3-MBA powder and (b) intermediate phases such as (PbI_2·3-MBA).

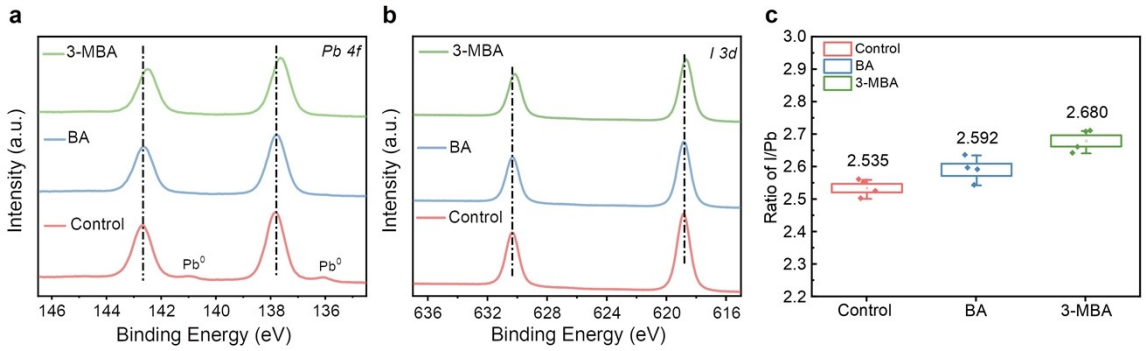

Figure S30. XPS spectra for (a) Pb 4f and (b) I 3d of the control, BA-, and 3-MBA-treated films. (c) The ratio of I/Pb estimated by XPS spectra on the surface of the control and modified perovskite films. In Pb 4f spectra, a significant binding energy shift is observed in the 3-MBA-treated perovskite film. In contrast, the BA-treated perovskite film exhibits a minor shift in binding energy to 142.64 eV (Δ=0.04 eV) for Pb $4f_{5/2}$ and 137.76 eV (Δ=0.05 eV) for Pb $4f_{7/2}$. This suggests that 3-MBA coordinates more strongly with Pb^{2+} in the perovskite structure compared to BA. Furthermore, the I 3d spectra exhibit a slight shift in the peaks representing I $3d_{3/2}$ and $3d_{5/2}$, exclusively in the 3-MBA-treated perovskite film. This might be attributed to the hydrogen bonding between -SH and I^-. Moreover, considering that the coordination bonding with Pb^{2+} in perovskite effectively suppresses the decomposition of PbI_6^{4-} framework into metallic Pb^0,[6] and I_2 under light and heat, the incorporation of 3-MBA effectively mitigated the formation of Pb^0, with binding energies assigned at 140.0 eV and 136.0 eV. We further quantified the amount of PbI_2 by estimating the average I:Pb ratio in perovskite films. This ratio was calculated from the integrated areas of the Pb $4f_{7/2}$ and I $3d_{5/2}$ peaks as shown in Table S7. The control and BA-treated samples exhibit an average I:Pb ratio of 2.535, and 2.592, respectively, while the 3-MBA-treated samples show a ratio of 2.680, a value close to 3. The increase in the I:Pb ratio clearly demonstrates that the 3-MBA remains to only a small amount of PbI_2 on the perovskite surface, as colloborated in Fig. 3b,c.

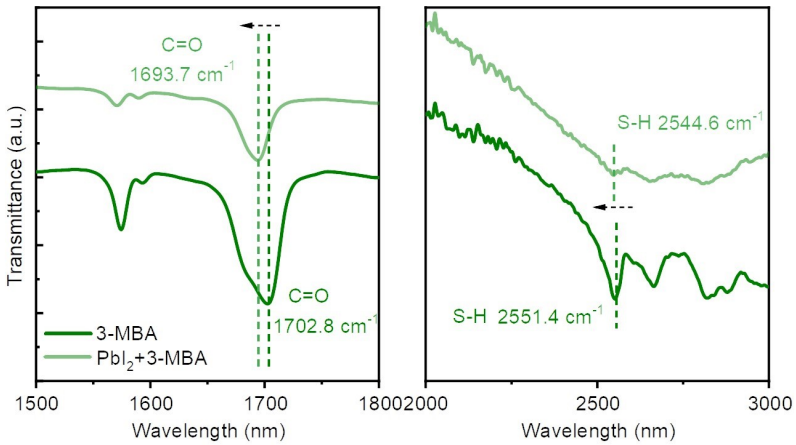

Figure S31. Fourier-transform infrared spectroscopy (FTIR) spectra of 3-MBA and 3-MBA-treated PbI_2 films. Following the addition of PbI_2, the C=O stretching vibrational peak shifted downward from 1702.8 to 1693.7 cm^{-1} upon adding PbI_2, indicative of electron donation to uncoordinated Pb^{2+} ions occurring in both Pb-O bonds. This implies that the carboxylate in D-3-MBA can induce a charge redistribution of positively localized charges at iodide vacancy. Concurrently, the thiol peak at 2551.4 cm^{-1} also shifted down to 2544.6 cm^{-1}, suggesting a hydrogen bonding interaction with I^-. This indicates that 3-MBA provides an effective passivator on divalent Pb^{2+} and potentially suppresses nonradiative recombination to be advantageous for achieving high-performance PSCs and stabilizing perovskite films.

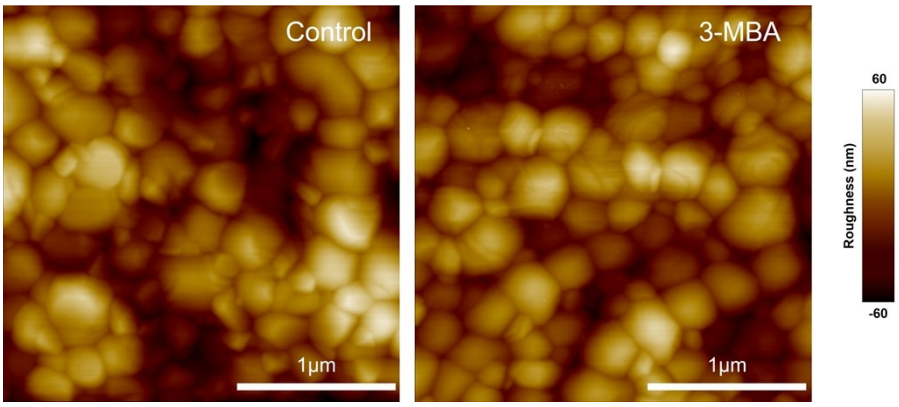

Figure S32. Atomic force microscopy (AFM) images of the perovskite films with and without 3-MBA treatment. The average roughness of the control and target films were 17.3 nm and 14.6 nm, respectively.

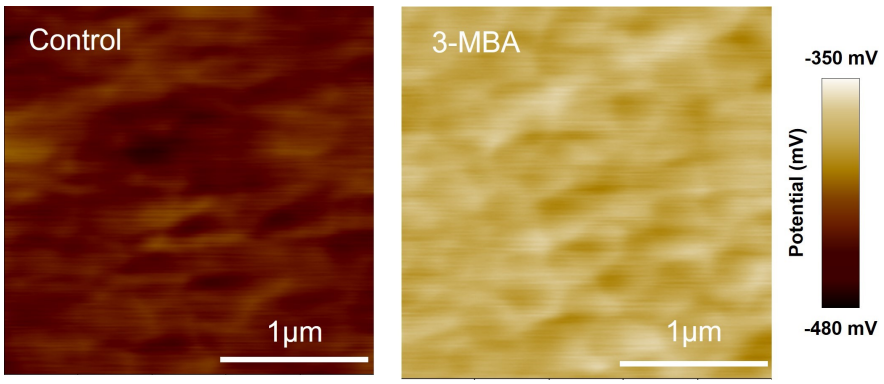

Figure S33. The kelvin probe force microscopy (KPFM) results for the with and without 3-MBA treatment.

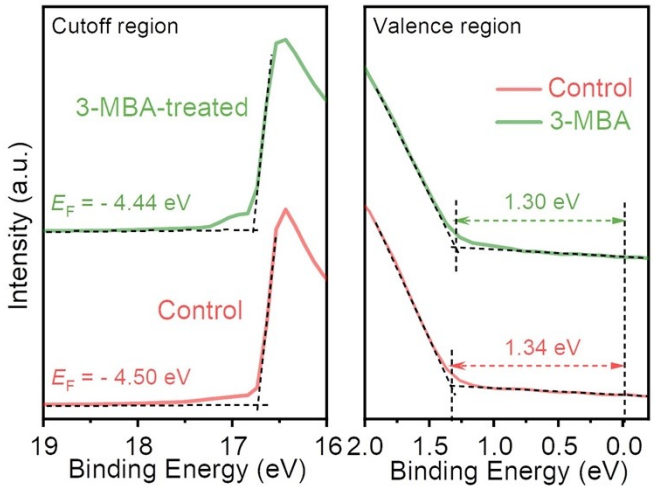

Figure S34. Ultraviolet photoelectron spectroscopy to estimate the band structure of the perovskite film with and without 3-MBA treatment.

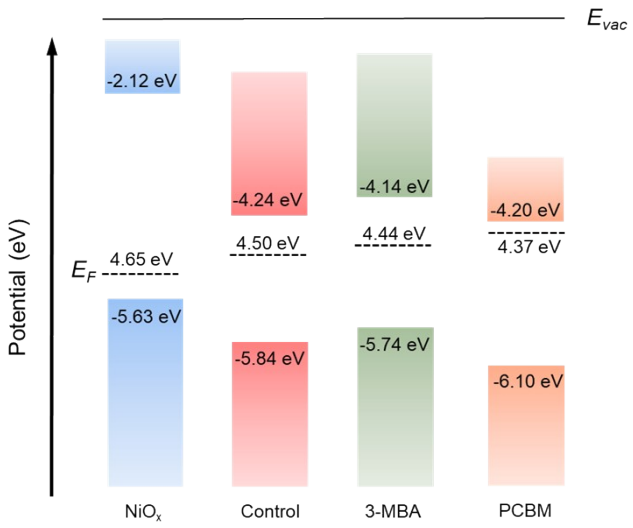

Figure S35. Energy-level scheme for the control and 3-MBA treated films.

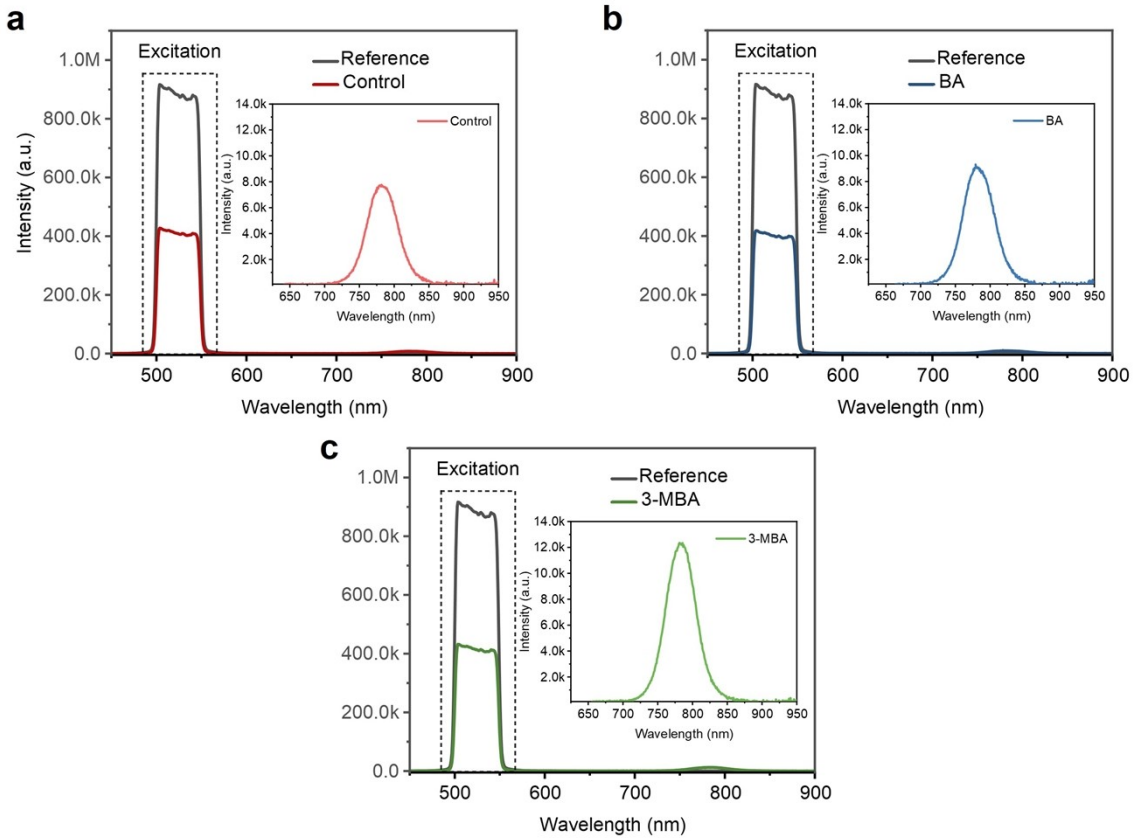

Figure S36. Absolute PL QY of (a) control and modified films with (b) BA and (c) 3-MBA.

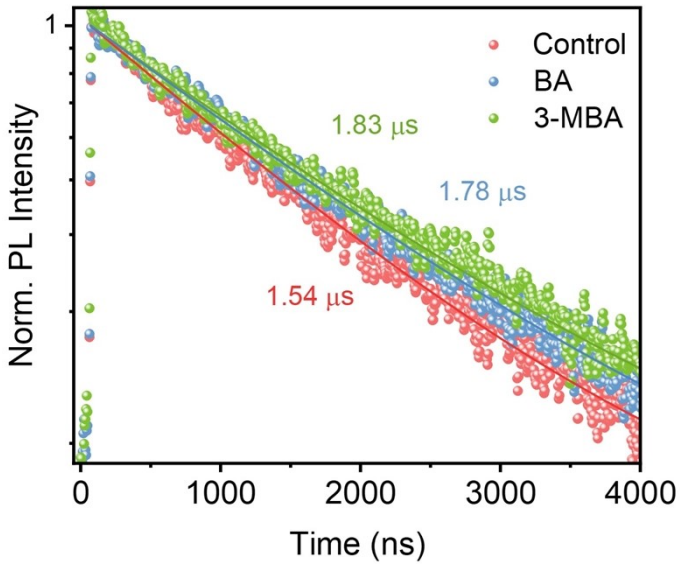

Figure S37. TRPL spectra of perovskite films of control, BA-, and 3-MBA-treated films.

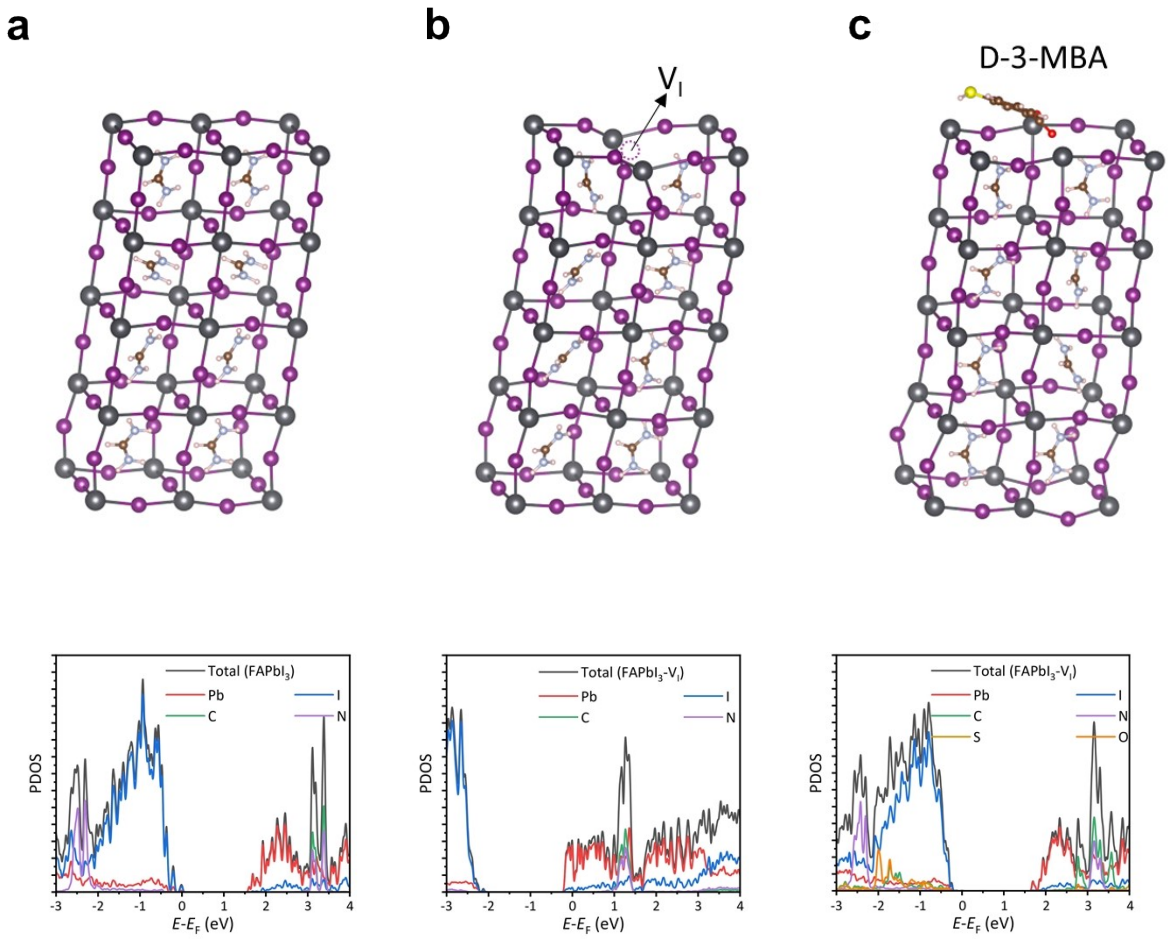

Figure S38. Optimized geometries of (a) pristine and iodide vacancy (V_I)-containing PbI_2-terminated (100) surface (b) without and (c) with D-3-MBA passivation, and their corresponding calculated projected Density of States (PDOS).

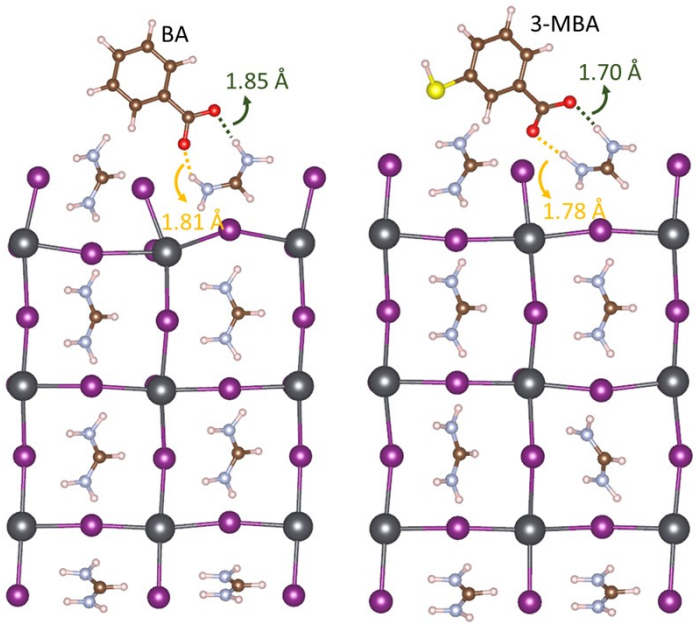

Figure S39. Optimized geometries of BA-absorbed (left) and 3-MBA-absorbed (right) on the FAI terminated (100) surface.

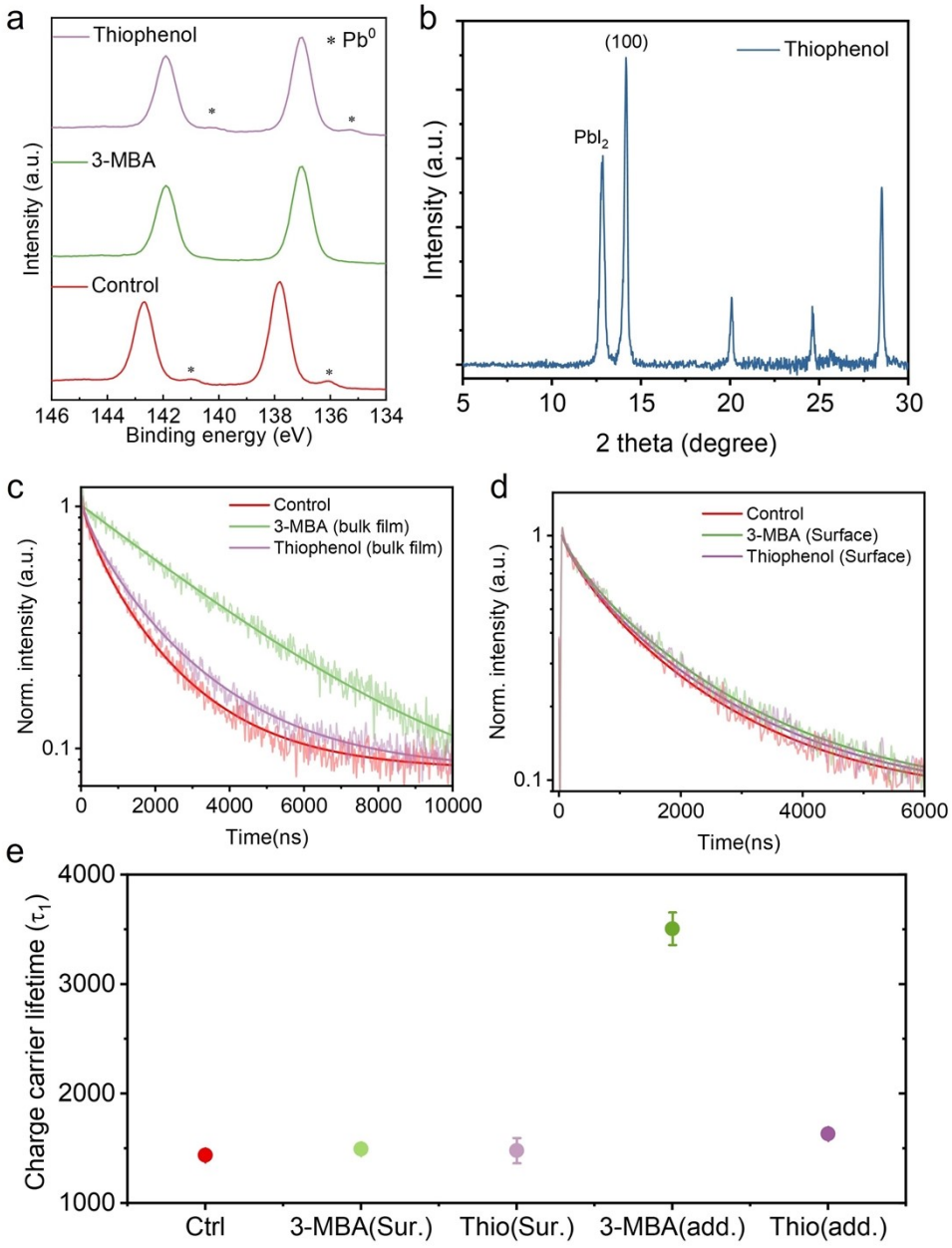

Figure S40. (a) XPS analysis of Pb 4f peaks in control, 3-MBA and thiophenol-added perovskite films. (b) XRD pattern of thiophenol-added perovskite film. (c) TRPL decay curves of perovskite films with additives (3-MBA and thiophenol) and without additive (control). (d) TRPL decay curves of perovskite films with surface treatments (3-MBA and thiophenol) and without treatment (control). (e) Corresponding charge carrier lifetimes (τ_1) fitted by monoexponential decay curve.

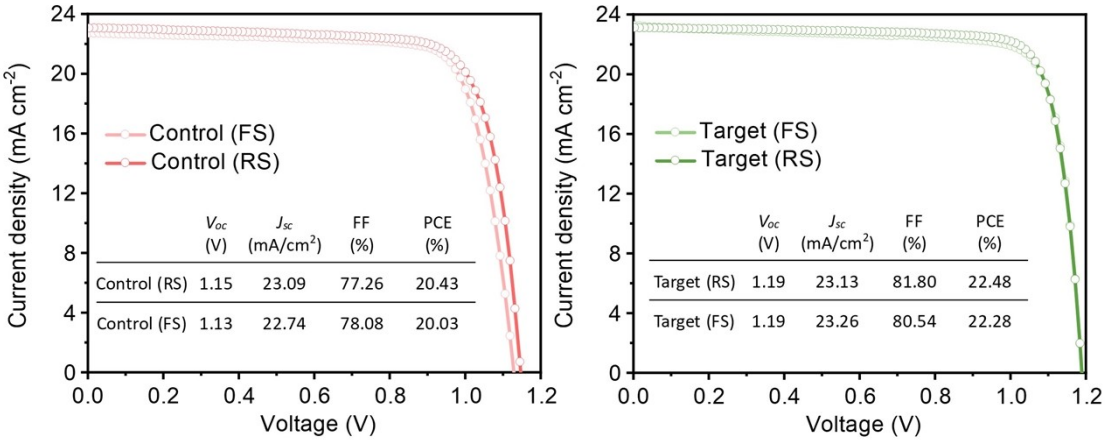

Figure S41. *J-V* curves for the control and 3-MBA-treated PSCs (perovskite E_g = 1.61eV). Hyteresis index is calculated from ($PCE_{reverse}$ – $PCE_{forward}$)/$PCE_{reverse}$.

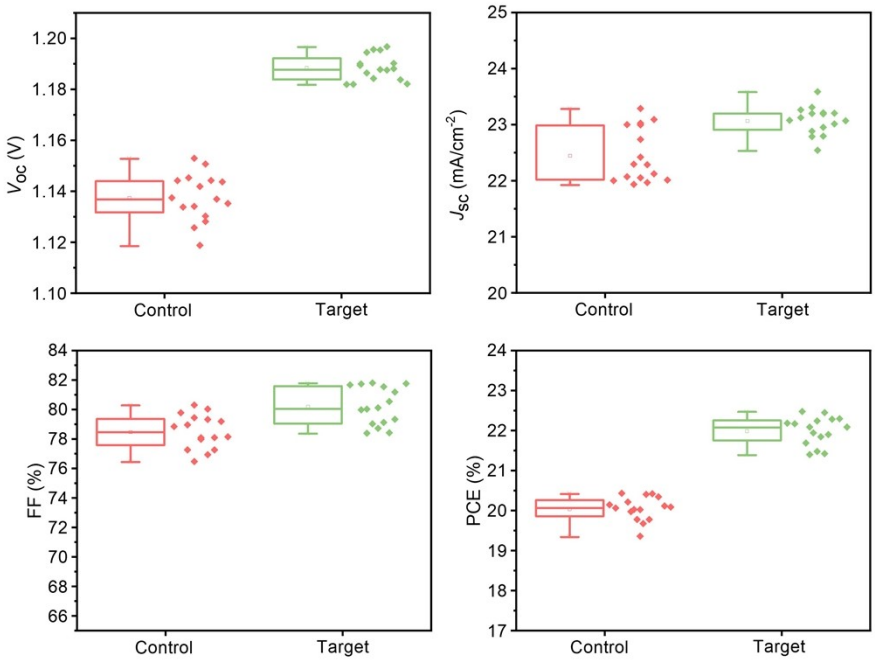

Figure S42. Histograms of Photovoltaic parameter (V_{oc}, J_{sc}, *FF*, and *PCE*) distributions (16 devices) (perovskite E_g = 1.61eV).

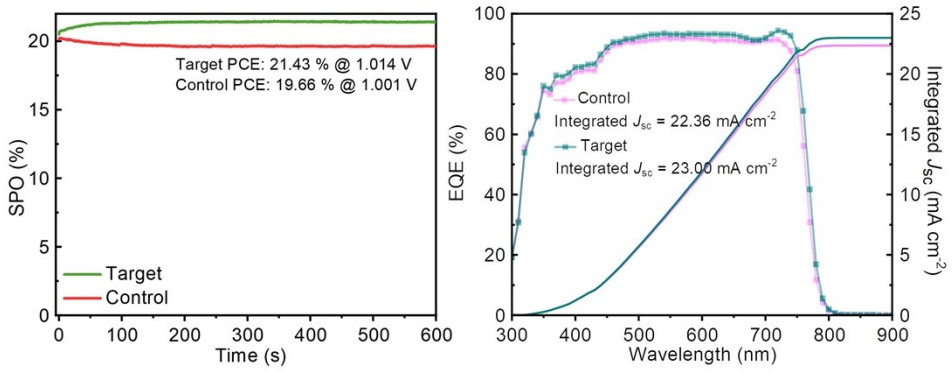

Figure S43. Stabilized power output and photocurrent measured at fixed biases of maximum power point. The external quantum efficiency (EQE) spectra and integrated short-circuit current density (J_{sc}) of the control and target PSCs (perovskite E_g = 1.61eV).

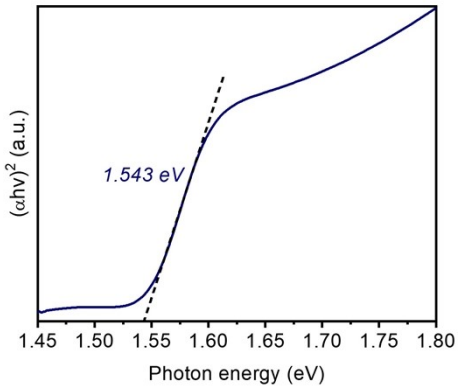

Figure S44. Bandgap estimation from the tauc plot (1.54 eV)

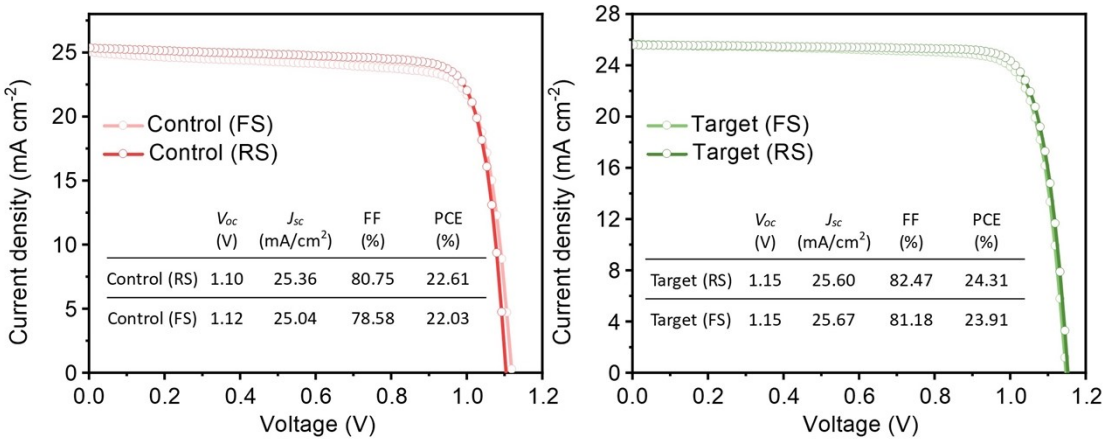

Figure S45. *J-V* curves for the control and 3-MBA-treated PSCs with bandgap ~1.54 eV perovskite film.

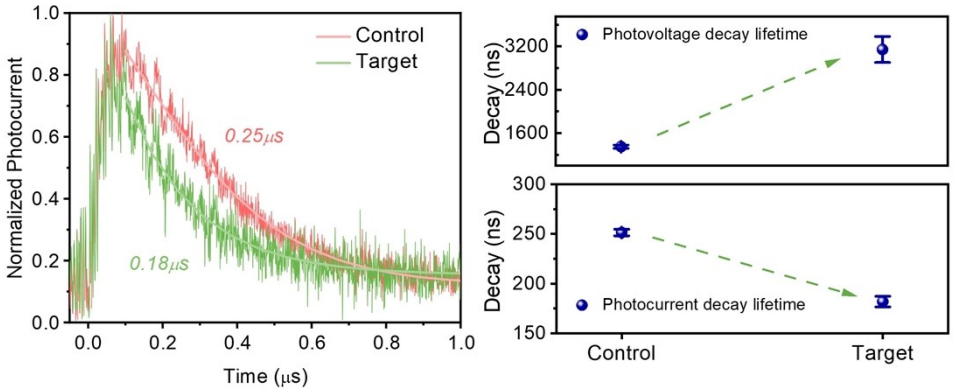

Figure S46. TPC curves of the control and target PSCs and average TPV and TPC decay lifetimes, where all data were collected for the individual 4 devices as average values ± standard deviation.

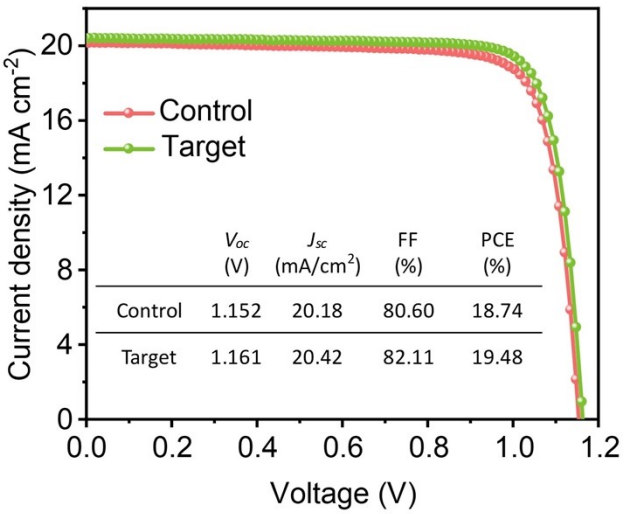

Figure S47. *J-V* curves for the control and 3-MBA-treated PSCs. The device configuration is a ITO/MeO-2PACz/Perovskite/C_{60}/SnO_2/Ag (perovskite composition is $Cs_{0.05}(FA_{0.85}MA_{0.15-})_{0.95}Pb(I_{0.85}Br_{0.15})_3$.

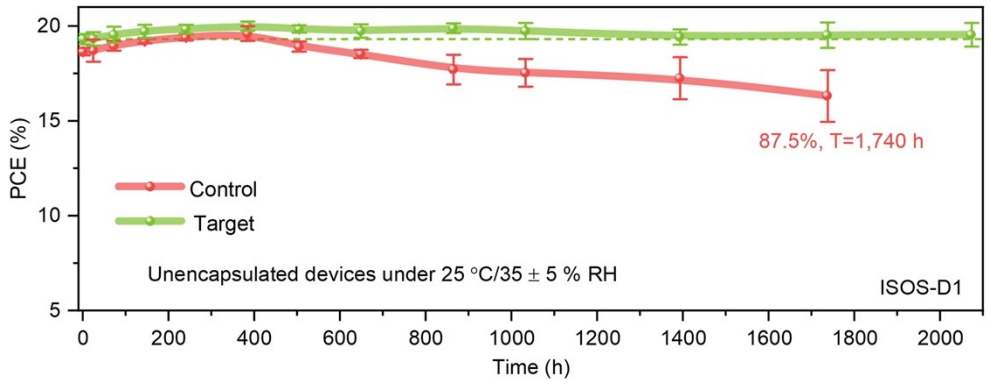

Figure S48. Long-term stability test stored at 25°C/RH of 35 ± 5%. All data are presented as average values ± standard deviation.

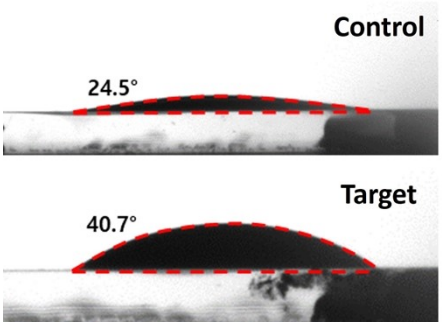

Figure S49. Water contact angles on surface of perovskite film with and without 3-MBA.

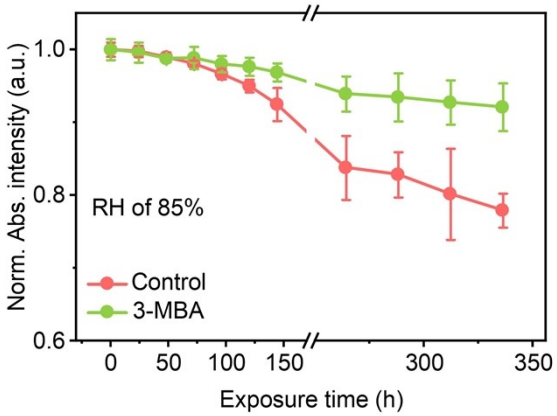

Figure S50. Evolution in absorption spectra (at 600 nm) of perovskite films of control, and 3-MBA-treated films for different exposure time under humidity aging at 85 ± 5% and 25 °C.

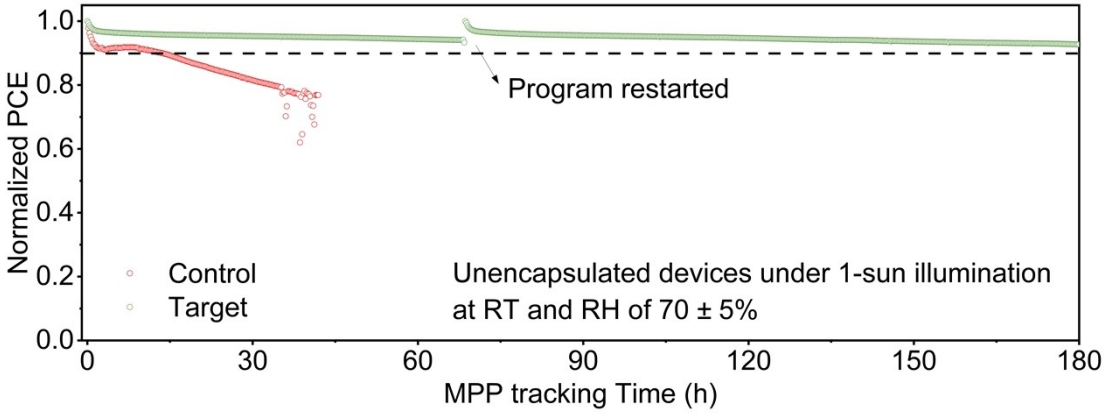

Figure S51. Operational stability test under high humidity at RT (~30 °C) and RH of 70 ± 5%

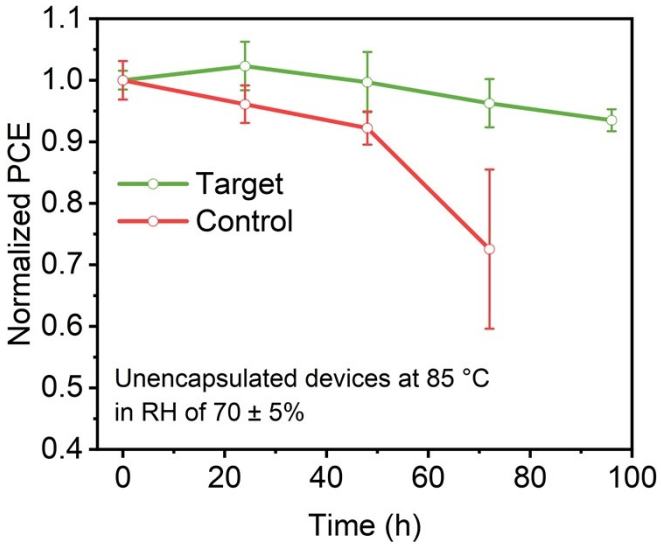

Figure S52. Thermal stability test at 85 °C under high humidity (RH of 70 ± 5%).

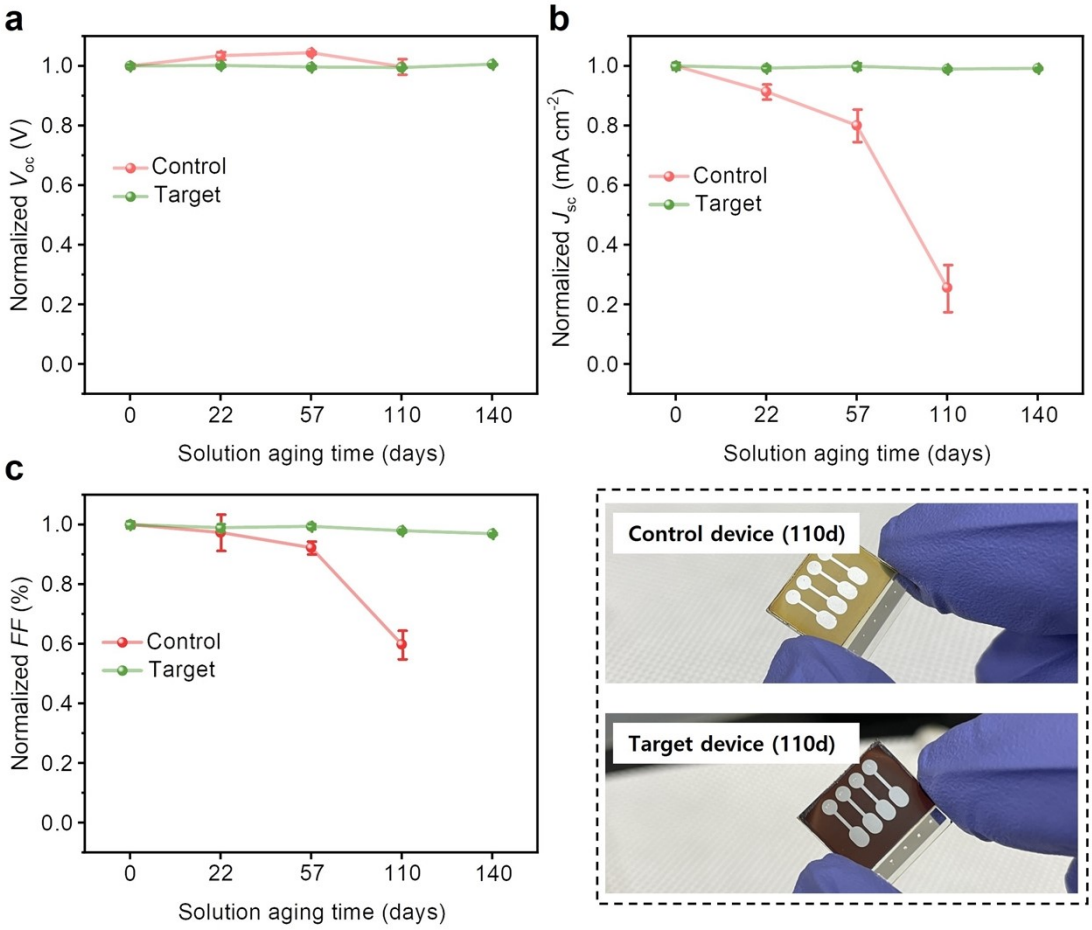

Figure S53. Evolution test of V_{oc}, J_{sc}, FF for the PSCs aged precursor based on strorage time with and without 3-MBA (control). All data are presented as average normalized values ± standard deviation. Device photographs of control and target devices using precursor with storage time for 110 d.

Table S1. Integration of peaks corresponding organic cation for 10 d-aged precursors, which is from the ^{1}H-NMR spectra.

Percentage (%)	*Left MA^+ (%)*	*Left FA^+ (%)*	*Generated MFA^+ (%)*	*Generated $DMFA^+$ (%)*
Control (pristine precursor)	88.4	96.8	3.7	0.4
3-MBA-incorporated precursor	99.9	99.5	0	0
BA-incorporated precursor	95.4	96.7	0.28	0

Table S2. Integration of peaks corresponding organic cation for 20 d-aged precursors, which is from the ^{1}H-NMR spectra.

Percentage (%)	*Left MA^+ (%)*	*Left FA^+ (%)*	*Generated MFA^+ (%)*	*Generated $DMFA^+$ (%)*
Control (pristine precursor)	82.0	91.4	6.8	0.6
3-MBA-incorporated precursor	98.8	99.2	0	0
BA-incorporated precursor	92.7	94.1	0.55	0

Table S3. Integration of peaks corresponding organic cation for 35 d-aged precursors, which is from the ^{1}H-NMR spectra.

Percentage (%)	*Left MA^+*	*Left FA^+*	*Generated MFA^+ (%)*	*Generated $DMFA^+$ (%)*
Control (pristine precursor)	73.7	86.2	11.3	1.1
3-MBA-incorporated precursor	98.4	99.8	0.6	0
BA-incorporated precursor	89.8	92.3	1.05	0

Table S4. Integration of peaks corresponding organic cation for 55 d-aged precursors, which is from the ^{1}H-NMR spectra.

Percentage (%)	*Left MA^+ (%)*	*Left FA^+ (%)*	*Generated MFA^+ (%)*	*Generated $DMFA^+$ (%)*
Control (pristine precursor)	66.3	79.0	24.8	2.5
3-MBA-incorporated precursor	97.6	99.2	1.0	0
BA-incorporated precursor	89.6	92.1	1.6	0.1

Table S5. Integration of peaks corresponding organic cation for 140 d-aged precursors, which is from the ^{1}H-NMR spectra.

Percentage (%)	*Left MA^+ (%)*	*Left FA^+ (%)*	*Generated MFA^+ (%)*	*Generated $DMFA^+$ (%)*
Control (pristine precursor)	7.5	12.9	75.9	8.4
3-MBA-incorporated precursor	93.1	95.1	1.7	0.2
BA-incorporated precursor	78.1	83.7	9.3	0.8

Table S6. Integration of peaks corresponding organic cation for thiophenol added precursors, which is from the ^{1}H-NMR spectra.

Percentage (%)	*Left MA^+ (%)*	*Left FA^+ (%)*	*Generated MFA^+ (%)*	*Generated $DMFA^+$ (%)*
0d	100	100	0	0
10d	86.6	92.2	1.9	0.2
20d	75.4	88.2	3.6	0.3
35d	75.0	86.8	6.6	0.6
55d	70.8	85.4	10.5	1.0

Table S7. I: Pb atomic ratio estimated by atomic ratio XPS spectra from individual 4 films.

	Control film	*3-MBA-modified film*	*BA-modified film*
I:Pb ratio	2.56101	2.70825	2.63596
	2.55253	2.71083	2.59147
	2.50232	2.64209	2.54359
	2.52513	2.66078	2.59649
Average	2.535 ± 0.027	2.680 ± 0.034	2.592 ± 0.038

Table S8. The Statistics of photovoltaic parameters of the control and target PSCs (~1.60 eV)

	V_{oc} (V)	J_{sc} (mA/cm^2)	*FF* (%)	*PCE* (%)
Control (Champion)	1.145	23.09	77.26	20.43
Control (Average)	1.138 ± 0.010	22.46 ± 0.48	78.50 ± 1.15	20.05 ± 0.30
Target (Champion)	1.188	23.13	81.80	22.48
Target (Average)	1.188 ± 0.005	23.07 ± 0.25	80.21 ± 1.28	22.00 ± 0.35

Table S9. The Statistics of photovoltaic parameters of the control and target PSCs (~1.54 eV)

	V_{oc} (V)	J_{sc} (mA/cm^2)	*FF* (%)	*PCE* (%)
Control (Champion)	1.104	25.36	80.75	22.61
Control (Average)	1.106 ± 0.006	25.12 ± 0.24	80.01 ± 0.71	22.23 ± 0.29
Target (Champion)	1.151	25.60	82.47	24.31
Target (Average)	1.139 ± 0.008	25.64 ± 0.18	81.29 ± 0.74	23.74 ± 0.29

Table S10. The Statistics of photovoltaic parameters of the PSCs with SnO_2 ALD as a buffer layer.

	V_{oc} (V)	J_{sc} (mA/cm^2)	*FF* (%)	*PCE* (%)
Control (Champion)	1.152	20.18	80.60	18.74
Control (Average)	1.150 ± 0.018	20.18 ± 0.09	80.10 ± 0.39	18.60 ± 0.11
Target (Champion)	1.161	20.42	82.11	19.48
Target (Average)	1.160 ± 0.004	20.37 ± 0.07	81.71 ± 0.27	19.31 ± 0.15

Note S1

The DFT calculation revealed that binding energy between D-3-MBA and FA^+ shows the highest value compared to the others (Figure S3). Moreover, it is worth noting that the other regioisomers (D-2-MBA and D-4-MBA) show weakened hydrogen bonding with FA^+ compared to the D-BA molecule (Fig. 1d in our manuscript), giving clear validity for the choice of meta-positioned 3-MBA. This further substantiates that 3-MBA can act as a target additive for hydrogen-mediated complexation and an effective modulator for perovskite devices with improved performance.

Note S2

DFT calculations revealed that D-3-MBA exhibits a stronger interaction with FA^+ than with Pb^{2+} (Figure S10). Naturally, when both PbI_2 and FAI are present in the solvent, the interactions become more complex due to the competition between I^- ions and the deprotonated carboxylate group for binding with Pb^{2+}. However, Pb^{2+} tends to bond more favorably with I^-, as the Pb-I interaction is generally stronger, making it unlikely for the carboxylate group to outcompete I^- through chelation. In addition, to determine the dominant interaction on perovskite films, we positioned the (110) facet with both the organic component (FA^+) and the inorganic cage (PbI_6^{4-} octahedral framework). We then evaluated the binding energy for the optimized geometries bonded with D-3-MBA (Figure S11). For case 1, D-3-MBA favorably binds with FA^+ through the hydrogen bonding and Pb^{2+} through a weak M-O coordination. While, for case 2, D-3-MBA favorably binds with Pb^{2+} through M-O coordination and FA^+ through relatively strong hydrogen bonding. Considering these cases, we found that the case 1 shows the higher binding energy than the case 2, which indicates that it is much stable that the D-3-MBA favorably interacts with FA^+ in perovskite film (Figure S11). In summary, we determined that D-3-MBA preferentially binds with FA^+ through hydrogen bonding rather than forming metal coordination with PbI_2. This finding is consistent across both molecular and perovskite surface models.

Note S3

After fresh perovskite precursor is made, the precursor is put into NMR tubes while being exposed to the RT of 25 ℃/RH of 40 ± 5%. Then, the precursor solution is continuously stored in the tubes with closed cover.

The percentages as to evolution of organic cations are estimated according to the previous work.[7]

$$Lost\ MA^+ = \frac{I_{MA^+(days)}}{I_{MA^+(fresh)}} = \frac{MA^+\ (days)}{CH_3\ of\ MA^+\ (fresh)}$$

$$Lost\ FA^+ = \frac{I_{FA^+(days)}}{I_{FA^+(fresh)}} = \frac{FA^+\ (days)}{CH\ of\ FA^+\ (fresh)}$$

$$Generated\ MFA^+ = \frac{I_{MFA^+(days)}}{I_{MA^+(fresh)}} = \frac{CH_3\ of\ MFA^+\ (days)}{CH_3\ of\ MA^+\ (fresh)}$$

$$Generated\ DMFA^+ = \frac{I_{DMFA^+(days)}}{I_{MA^+(fresh)}} = \frac{CH_3\ of\ DMFA^+\ (days)}{CH_3\ of\ MA^+\ (fresh)}$$

Note S4

Following the definition of the acid dissociation constant (pK_a), The MA^+ with a relatively low pK_a value of 10.66 possesses ability to readily deprotonate among the various cation groups generally used as A-sites in perovskite composition (basically follows as; ABX_3).[8]

$$pK_a(A^+) = -\log_{10}\frac{[A^0][H^+]}{[A^+]}$$

$$MA^+ \leftrightarrow MA^0 + H^+$$

Where, $[A^0]$, $[H^+]$, and $[A^+]$ are the equilibrium concentrations of A^0, H^+, and A^+, respectively. According the the equation, ability to dissociate H^+ can be suppressed following the reversible equilibrium process. In other words, taken with the reaction as mentioned above, the endowed protons (H^+) can effectively mitigate the deprotonation of MA^+ as reported in previous study (reversible equilibrium ionization).[7] Moreover, because the acid dissociation shows the endothermic process, the deprotonation is further accelerated at high temperature, which implys that the lowering the temperature of perovskite precursors with MA^+ component would be also beneficial for their degradation.[9]

Note S5

To generate iodine (I_2), the solutions with and without 3-MBA are kept in open cover for 15 h at 60 ℃ and RH of 40-50% and continuously stirred using magnetic bar. 0.01M of 3-MBA and BA are incorporated in 1.0M of FAI, respectively (DMF:solvent).

Note S6

Calculation of the work function by Kelvin probe force microscopy (KPFM) results

The surface potential from the KPFM results, termed as contact potential difference (CPD) between tip and sample are calculated as follows;

$$CPD = \frac{\Phi_{tip} - \Phi_{sample}}{e}$$

Where, Φ_{tip} and Φ_{sample} are the work functions of tip and sample on surface, respectively.

Note S7

Time-resolved photoluminescence (TRPL) decay curve fitting

The TRPL decay curves are fitted according to the mono-exponential equation only to define the pathway to radiative recombination where electron and hole recombine within bulk perovskite;

$$f(t) = A_1 exp\left(\frac{-t}{\tau_1}\right)$$

Where, A_1 is the relative amplitude, and τ_1 represents bimolecular carrier decay time, respectively.

Note S8

Influence of treating Thiophenol on surface and bulk films.

We have conducted the XPS analysis of thiophenol-added perovskite film. As shown in Fig. S40a, we observed a shift in the Pb 4f peaks after adding thiophenol and 3-MBA to the bulk films (at equivalent molar concentrations as mentioned in supplementary information), indicating interactions with uncooridnated Pb^{2+}.[10] However, metallic Pb^0 peaks (at 140.2 and 135. 2 eV) were still oberved in the thiophenol-added film. In addition, we performed TRPL analysis to assess the passivation ability of thiophenol on both the surface and bulk films (Fig. S40c and d). For surface treatment, an equivalent concentration of 0.01 M in IPA solvent was applied on perovskite surface. Notably, all thiophenol-treated perovskite film, whether treated on the surface or in bulk, exhibited improved carrier lifetimes compated to the control film (Fig. S40e). This suggests that thiophenol effectively passivates uncoordinated Pb^{2+} (as illustrated by XPS spectrum of Pb 4f peaks for thiophenol), potentially enhancing the stability of the film.

Despite the beneficial passivation effect of thiophenol on perovskite, we are concerned that thiophenol may also contribute to the degradation of the perovskite. While thiophenol can bind to uncoordinated Pb^{2+}, passivating defect states and suppressing nonradiative recombination, it has been observed that adding thiophenol leaves a significant amount of PbI_2 in the perovskite film as shown in XRD spectra (see Fig. S40b and compare it with Fig. 3c, a similar phenomenon has also been observed in a previous report.[11] In addition, as confirmed by XPS analysis (Fig. S40a), metallic Pb^0 was detected in the thiophenol-added films. It is well known that PbI_2 tends to decompose into metallic lead (Pb^0) and I_2 under light exposure, which accelerates the degradation of the films.

In summary, thiophenol treatments on the surface and in bulk films have effectively contributes to the passivation of defect states such as uncoordinated Pb^{2+} (i.e., iodide vacancies). In 3-MBA treatment, however, cooridination effect is dominated by carboxylate group, where thiol

functional group only supports acting as both an electron-donating and anchoring group (with I^-), demonstrated in DFT calculation (Fig. 3g).

We also highlight that thiophenol treatment in bulk films leaves a significant amount of unreacted PbI_2, which promotes metal-mediated degradation under light exposure (as the films are inevitably exposed to continuous X-ray radiation during XPS analysis), not occuring in 3-MBA treatment shown in Fig. 3c and d.

Note S9

V_{oc} vs light intensity

The ideal factor (n) corresponding the slope of the curve is calculated by the following equation:

$$n = \frac{e \quad dV_{oc}}{k_B T d\ln(I)}$$

Where, k_B, T, and I are the Boltzmann constant, temperature, and light intensity, respectively.

Note S10

TPV and TPC analysis

The TPV and TPC data were fitted by a mono-exponential method as a function of time for charge recombination and charge extraction.

$$I(t) = A_1 exp\left[-\left(\frac{t}{\tau}\right)\right]$$

Here, I(t) is the PL intensity as a function of time, τ is the charge lifetime, and A_1 is the amplitude ratio. The TPV and TPC measurement were conducted by a Nd:YAG laser (SLII-10) excitation source as a perturbation light, tuned to a wavelength of 532 nm (10 Hz, with pulse duration <4 ns) and Xe lamp (150 W, ABET tech) is further used as a bias light source. The intensity of the laser was adjusted to keep ΔV smaller than 20 mV. The bias light intensity was fixed in 1 sun. Wherein, the transient voltage and current were recorded using a digital oscilloscope (300 MHz, DPO 3032, Tektronix) under open circuit and short circuit conditions with 1 MΩ and 50 Ω resistors, respectively.

References

1. S. Ko, T. Yong, S.-K. Kim, J. Y. Park, G. Lee, H. R. You, S. Han, D. H. Lee, S. Choi, Y. C. Choi, Y. Kim, N.-S. Lee, S. Song and J. Choi, *Sol. RRL*, 2023, **7**, 2300049.
2. X. Wang, Y. Fan, L. Wang, C. Chen, Z. Li, R. Liu, H. Meng, Z. Shao, X. Du, H. Zhang, G. Cui and S. Pang, *Chem*, 2020, **6**, 1369-1378.
3. G. J. Corban, C. D. Antoniadis, S. K. Hadjikakou, N. Kourkoumelis, V. Y. Tyurin, A. Dolgano, E. R. Milaeva, M. Kubicki, P. V. Bernhardt, E. R. T. Tiekink, S. Skoulika and N. Hadjiliadis, *Heteroat. Chem.*, 2012, **23**, 498-511.
4. G. Lu, W. Zhu, F. He, D. Chen, C. Zhang and Y. Hao, *Mater. Lett.*, 2019, **250**, 88-91.
5. N. K. Noel, M. Congiu, A. J. Ramadan, S. Fearn, D. P. McMeekin, J. B. Patel, M. B. Johnston, B. Wenger and H. J. Snaith, *Joule*, 2017, **1**, 328-343.
6. F. Li, X. Deng, F. Qi, Z. Li, D. Liu, D. Shen, M. Qin, S. Wu, F. Lin, S.-H. Jang, J. Zhang, X. Lu, D. Lei, C.-S. Lee, Z. Zhu and A. K. Y. Jen, *J. Am. Chem. Soc.*, 2020, **142**, 20134-20142.
7. M. Li, H. Li, Q. Zhuang, D. He, B. Liu, C. Chen, B. Zhang, T. Pauporté, Z. Zang and J. Chen, *Angew. Chem. Int. Ed.*, 2022, **61**, e202206914.
8. M. Wang, Z. Shi, C. Fei, Z. J. D. Deng, G. Yang, S. P. Dunfield, D. P. Fenning and J. Huang, *Nat. Energy*, 2023, **8**, 1229-1239.
9. M. E. O'Kane, J. A. Smith, T. I. Alanazi, E. J. Cassella, O. Game, S. van Meurs and D. G. Lidzey, *ChemSusChem*, 2021, **14**, 2537-2546.
10. C. Li, X. Wang, E. Bi, F. Jiang, S. M. Park, Y. Li, L. Chen, Z. Wang, L. Zeng, H. Chen, Y. Liu, C. R. Grice, A. Abudulimu, J. Chung, Y. Xian, T. Zhu, H. Lai, B. Chen, R. J. Ellingson, F. Fu, D. S. Ginger, Z. Song, E. H. Sargent and Y. Yan, *Science*, 2023, **379**, 690-694.
11. B. P. Finkenauer, Y. Zhang, K. Ma, J. W. Turnley, J. Schulz, M. Gómez, A. H. Coffey, D. Sun, J. Sun, R. Agrawal, L. Huang and L. Dou, *J. Phys. Chem. C*, 2023, **127**, 930-938.